NASA/TM–2019-220260

Characterization of 10-ft. Diameter Aluminum Alloy 2219 Integrally Stiffened Cylinders

Wesley A. Tayon, Marcia S. Domack , and John A. Wagner
Langley Research Center, Hampton, Virginia

March 2019

NASA STI Program . . . in Profile

Since its founding, NASA has been dedicated to the advancement of aeronautics and space science. The NASA scientific and technical information (STI) program plays a key part in helping NASA maintain this important role.

The NASA STI program operates under the auspices of the Agency Chief Information Officer. It collects, organizes, provides for archiving, and disseminates NASA's STI. The NASA STI program provides access to the NTRS Registered and its public interface, the NASA Technical Reports Server, thus providing one of the largest collections of aeronautical and space science STI in the world. Results are published in both non-NASA channels and by NASA in the NASA STI Report Series, which includes the following report types:

- TECHNICAL PUBLICATION. Reports of completed research or a major significant phase of research that present the results of NASA Programs and include extensive data or theoretical analysis. Includes compilations of significant scientific and technical data and information deemed to be of continuing reference value. NASA counter-part of peer-reviewed formal professional papers but has less stringent limitations on manuscript length and extent of graphic presentations.

- TECHNICAL MEMORANDUM. Scientific and technical findings that are preliminary or of specialized interest, e.g., quick release reports, working papers, and bibliographies that contain minimal annotation. Does not contain extensive analysis.

- CONTRACTOR REPORT. Scientific and technical findings by NASA-sponsored contractors and grantees.

- CONFERENCE PUBLICATION. Collected papers from scientific and technical conferences, symposia, seminars, or other meetings sponsored or co-sponsored by NASA.

- SPECIAL PUBLICATION. Scientific, technical, or historical information from NASA programs, projects, and missions, often concerned with subjects having substantial public interest.

- TECHNICAL TRANSLATION. English-language translations of foreign scientific and technical material pertinent to NASA's mission.

Specialized services also include organizing and publishing research results, distributing specialized research announcements and feeds, providing information desk and personal search support, and enabling data exchange services.

For more information about the NASA STI program, see the following:

- Access the NASA STI program home page at http://www.sti.nasa.gov

- E-mail your question to help@sti.nasa.gov

- Phone the NASA STI Information Desk at 757-864-9658

- Write to:
  NASA STI Information Desk
  Mail Stop 148
  NASA Langley Research Center
  Hampton, VA 23681-2199

NASA/TM–2019-220260

Characterization of 10-ft. Diameter Aluminum Alloy 2219 Integrally Stiffened Cyclinders

Wesley A. Tayon, Marcia S. Domack, and John A. Wagner
Langley Research Center, Hampton, Virginia

National Aeronautics and
Space Administration

Langley Research Center
Hampton, Virginia 23681-2199

March 2019

Available from:

NASA STI Program / Mail Stop 148
NASA Langley Research Center
Hampton, VA 23681-2199
Fax: 757-864-6500

LIST OF ACRONYMS, SYMBOLS, DESIGNATORS, AND ABBREVIATIONS

A	Axial
AF	As-Formed
AMS	Aerospace Metals Specification
ANNST	Advanced Near Net Shape Technology
ASTM	American Society for Testing and Materials
C	Circumferential
CBA	Cost-Benefit Analysis
GCD	Game Changing Development
ε	True Strain
e_{max}	Maximum Elongation
$e_{uniform}$	Uniform Elongation
EDM	Electrical Discharge Machining
EDS	Energy Dispersive Spectroscopy
HT1	Heat Treatment #1
HT2	Heat Treatment #2
IML	Inner Mold Line
ISC	Integrally Stiffened Cylinder
ksi	Thousand Pounds per Square Inch
LaRC	Langley Research Center
$\dot{m}$	Material flow rate
n	Strain Hardening Exponent
OML	Outer Mold Line
r	Plastic Strain Ratio
R	Radial
σ	True Stress
SEM	Scanning Electron Microscopy
SHT	Solution Heat Treatment
t	Thickness
UTS	Ultimate Tensile Strength (measured in ksi)
w	Width
YS	0.2 % Offset Yield Strength (measured in ksi)

Abstract

The integrally stiffened cylinder (ISC) process, pioneered by NASA Langley Research Center, offers significant savings for launch vehicle structures. The ISC process is a near net shape, advanced manufacturing method for fabrication of single-piece, thin-walled barrels with internal longitudinal stiffeners, eliminating the need for longitudinal welding and machining. A cost-benefit analysis of the ISC process estimated a 50 % reduction in manufacturing costs and a 10% weight savings over the current multi-piece, machined and welded construction approach for stiffened barrels. In 2017, commercial-scale manufacturing trials were pursued, leading to a successful manufacturing demonstration of 10-ft. diameter ISC barrels fabricated from Al alloy 2219. Some cracking was observed in the stiffeners during fabrication. Optical metallography was performed to evaluate the as-formed microstructures to identify potential causes of cracking, along with mechanical testing to evaluate formability. Results revealed that cracking in the stiffeners was attributed to three likely causes: 1) large Al-Cu stringer particles, 2) stick-slip friction between the mandrel and ISC due to non-optimized lubrication, and 3) differences in material flow rate between the wall and stiffener locations. Testing to gauge formability revealed a significant decrease in ductility in the longitudinal directional for the as-formed condition, attributed to reduced ductility due to the large Al-Cu stringer particles. These results provide guidance toward materials and processing modifications for future ISC forming trials.

Keywords: Integrally Stiffened Cylinder (ISC) Process; advanced manufacturing; near net shape; cryogenic tanks; Al alloy 2219

1. Introduction

The current fabrication method for launch vehicle structures, such as cryogenic propellant tanks, is multi-piece machined and welded construction. This method has been used since the 1950's. The Advanced Near Net Shape Technology (ANNST) Project under NASA's Game Changing Development (GCD) Program Office is developing a new manufacturing method, known as the integrally stiffened cylinder (ISC) process, which offers a significant reduction of cost and weight for future cryotank fabrication. The key to the ISC process is the demonstrated ability to simultaneously form the barrel wall and stiffeners in a single forming operation.

A cost-benefit analysis (CBA) study was undertaken in 2015 at NASA Langley Research Center (LaRC) to quantify the benefits of the ISC process over conventional, multi-piece welded construction for fabrication of cryogenic tank barrel sections [1]. For the CBA, a hypothetical tank size of 16 feet in diameter by 40 feet in length was selected, which is within the size range of commercial launch vehicles in the US. The CBA showed that labor costs accounted for ~ 60 % of the total manufacturing cost for the conventional manufacturing approach. By comparison, the CBA study estimated that the ISC process could reduce manufacturing cost by 50 % compared to the conventional multi-piece approach. This savings is due to reducing the labor for machining and inspection, thereby reducing the manufacturing schedule by 60 %. Mass savings for the ISC process were estimated to range from 5 - 10 % due simply to eliminating longitudinal welds and weld lands. Further mass reduction is possible through design optimization to capitalize on new cryogenic tank designs enabled by the ISC process.

The ISC process is a single-step metal flow-forming operation, which creates integral longitudinal stiffeners on the inner mold line (IML) surface of a cylinder as depicted in Figure 1. During the process, a thick-walled preform is flow-formed over a cylindrical mandrel, which has grooves machined on the outer mold line (OML) surface that correspond to the desired stiffener shape. Both the mandrel and preform are spinning during forming. Forming occurs at room temperature with no active heating or cooling; however, there is some part heating due to friction. Multiple pairs of counter rollers that spin and translate in the axial direction provide the necessary mechanical force to facilitate the forming process. The position of the rollers about the circumferential direction is fixed. The internal rollers provide support for the hollow mandrel. The external forming rollers exert force against the outer wall of the preform, extending the length of the cylinder and reducing the wall thickness, while simultaneously forcing material into the mandrel grooves to form the stiffeners. The number and geometry of the grooves in the mandrel can be tailored for the desired longitudinal stiffener configuration and spacing in the final part.

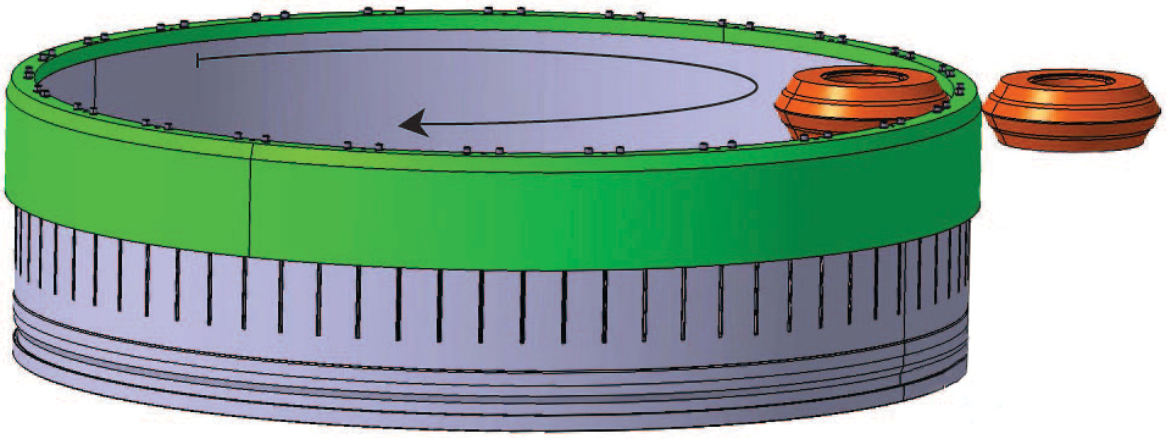

Figure 1. ISC manufacturing process schematic at 10-ft. diameter scale depicting the mandrel (gray), the preform (green), and the rollers (red). Arrow indicates clockwise mandrel rotation direction. (Drawing adapted with permission from MT Aerospace)

The ISC process development began with a successful demonstration of an 8-inch diameter aluminum cylinder in 2012. In 2015, the process was scaled up to a diameter of 17 inches, ultimately producing an ISC that was flown on a sounding rocket in collaboration with NASA Wallops Flight Facility [2]. Under ANNST, NASA is working with an international team, detailed below, to scale the process up to 10 ft. in diameter, which is relevant to current launch vehicle designs within US industry and the European Space Agency (ESA).

In 2017, the ANNST team led the first forming campaign at the 10-ft. diameter scale. Three 10-ft. diameter Al 2219 preform rings, like the one shown in Figure 1, were produced in the US at Scot Forge (Spring Grove, IL). Fabrication of the cylinders occurred at MT Aerospace (Augsburg, Germany) in collaboration with ESA and Lockheed Martin Space Systems (Littleton, CO) with guidance from the ANNST team. ESA-owned equipment for commercial production of Ariane 5 booster segments was modified during a 3-month production stoppage window to facilitate forming trials using the ISC process. This equipment was originally designed and used solely for the purpose of fabricating smooth-wall steel cylinders, and not optimized for the ISC process. A dedicated ISC machine was estimated to cost $8 M [1]. Lessons learned from this forming campaign will be used to guide future development of ISC forming equipment.

The ANNST team also provided guidance on mandrel design. The mandrel used for the 10-ft. diameter forming trials is shown in Figure 2. The forming equipment can be seen in the background behind the mandrel. The mandrel had a total of 48 equally-spaced grooves of two different shapes, three depths, and two widths (a total of 12 unique combinations), repeated four times about the circumference. The stiffeners on the formed ISC part take the shape of the grooves on the mandrel. Non-proprietary details regarding these 12 groove configurations labeled A-L are shown in Table 1. Specific details regarding the shape of the grooves are considered proprietary and cannot be provided. However, generically speaking, shape 1 was a symmetric groove and shape 2 was a non-symmetric groove about the centerline of the stiffener in the radial direction (direction of stiffener fill).

Figure 2. 10-ft. diameter ISC mandrel and forming equipment seen behind the mandrel. (Image used with permission from MT Aerospace)

Table 1. Groove designations and dimensions in inches.

Stiffener	A	B	C	D	E	F	G	H	I	J	K	L
Width	0.24	0.24	0.24	0.32	0.32	0.32	0.24	0.24	0.24	0.32	0.32	0.32
Depth	1.0	0.8	0.6	1.0	0.8	0.6	1.0	0.8	0.6	1.0	0.8	0.6
Shape	1	1	1	1	1	1	2	2	2	2	2	2

During forming, the mandrel and preform spin in unison and the rollers are at fixed circumferential positions. Consequently, material flowing along one side of the groove sees contact from the roller first. As depicted in Figure 3, this leads to the concept of an “upstream” and “downstream” side for the groove and stiffener. The rotation of the mandrel combined with the axial and radial translation of the roller causes an asymmetric flow of material into the groove such that the

upstream side fills first, which has implications for material and friction effects that will be discussed in the results section.

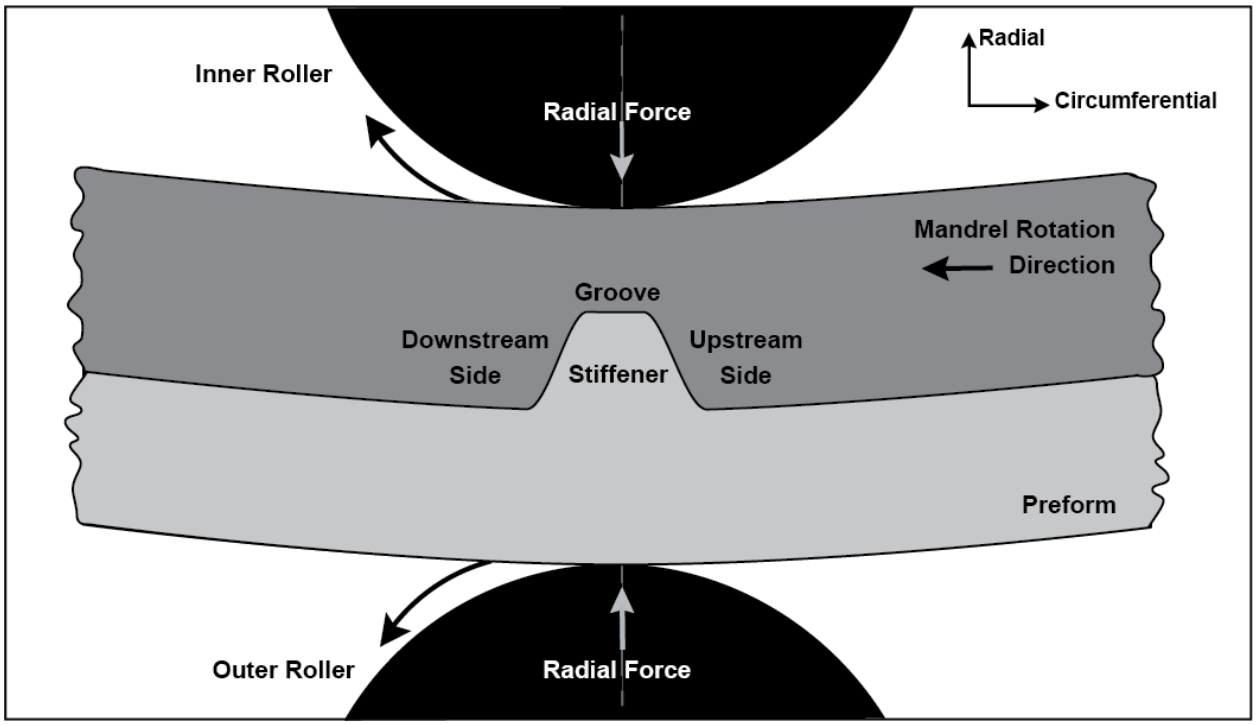

Figure 3. Sketch to illustrate concept of an "upstream" and "downstream" side of stiffener and groove in relation mandrel and roller rotation.

During the 2017 forming campaign, ANNST successfully demonstrated the manufacturing feasibility of the ISC process at the 10-ft. diameter scale. However, a defect-free ISC was not produced due to some cracking issues primarily within the stiffeners. Under ANNST, characterization of the 10-ft. diameter ISCs was led by NASA LaRC. This characterization included metallurgical evaluation and mechanical testing to better understand the process and determine potential causes of the cracking observed. Additionally, heat treatment studies were performed to evaluate and improve material formability for future forming activities.

2. Materials and Processing

Multiple segments from the 10-ft. diameter ISCs were sectioned and prepared for metallurgical analysis. These ISCs were fabricated from ring preforms made from aluminum alloy Al 2219, a nominally Al – 6wt.% Cu alloy with heritage for use in launch vehicle structures. It is worth noting that 6 wt.% Cu is in excess of the solubility limit for Cu in Al (Cu has 5.65 wt.%. solubility in Al [3]), leading to the formation of a certain volume fraction of phases that will likely not fully dissolve during heat treatment. However, particle size and morphology may be altered through partial dissolution.

The preform production process starts with upset forging an ingot, which is then pierced to facilitate forging operations to expand the diameter. Finally, the diameter is further expanded on a dedicated ring rolling machine. At the conclusion of ring rolling, the rings were annealed at 775 °F for 3.75 hours to produce an O-temper condition. The rings were machined to final nominal dimensions of 10-ft. inner diameter by 14.5 inches tall by 3 inches thick. Two of the ring preforms are shown in Figure 4.

Figure 4. Two ISC ring preforms as delivered to MT Aerospace. (Image used with permission from MT Aerospace)

A total of five forming trials (referred to as test numbers 1-5) were completed with Al 2219. Photographs are shown in Figure 5 and Figure 6 illustrating key test results. Test #1 exhibited widespread cracking and the test was suspended quickly to avoid damaging the machine. The remaining unformed region of the test #1 preform was cut off and used as the starting preform for test #2. Test #2 was conducted at elevated temperature of ~ 175 °F by preheating the preform before installation on the mandrel. The process became unstable due to diametrical expansion of the preform resulting in loss of contact with the mandrel; consequently, stiffeners were not able to be formed. Test #3 was the most successful of the 5 attempts, resulting in the least cracking and best fill of the stiffeners, and most extension of the cylinder. The improved forming from test #1 to test #3 is shown in Figure 5. The largest change to process parameters from test #1 to 3 was an increase in the roller axial translation speed by roughly 1.5 to 2x (exact processing parameters are proprietary). During fabrication, audible signs of cracking could be heard, but forming continued leading to some of the large cracks extending into the wall as shown in Figure 5. For test #4, parameters remained that same as test #3, but it was predetermined that forming would be suspended at the first sound of cracking in order to identify where cracking initiates. Cracking occurred relatively early in the forming trial, hence there was remaining unformed material from the test #4 preform that was removed and used as the starting preform for test #5. Similar to the re-use of preform material for test #2, test #5 was also unsuccessful due to process instability and subsequent diametrical growth; no stiffeners were formed. Test #2 and 5 suggest that the re-use of shortened preforms does not provide adequate material to reach steady state forming, causing failure to reach a stable processing condition required for stiffener fabrication. A comparison of one of the best formed stiffeners from tests #1, 3, and 4 are shown side by side in Figure 6. This highlights the greater stiffener extension achieved in test #3 with process parameter adjustments. Test #4 clearly demonstrated that cracking initiated in the stiffeners and that stopping the process at the first sound of cracking prevented subsequent tearing in the wall.

Figure 5. OML views providing comparison of improved success from test #1 to test #3.

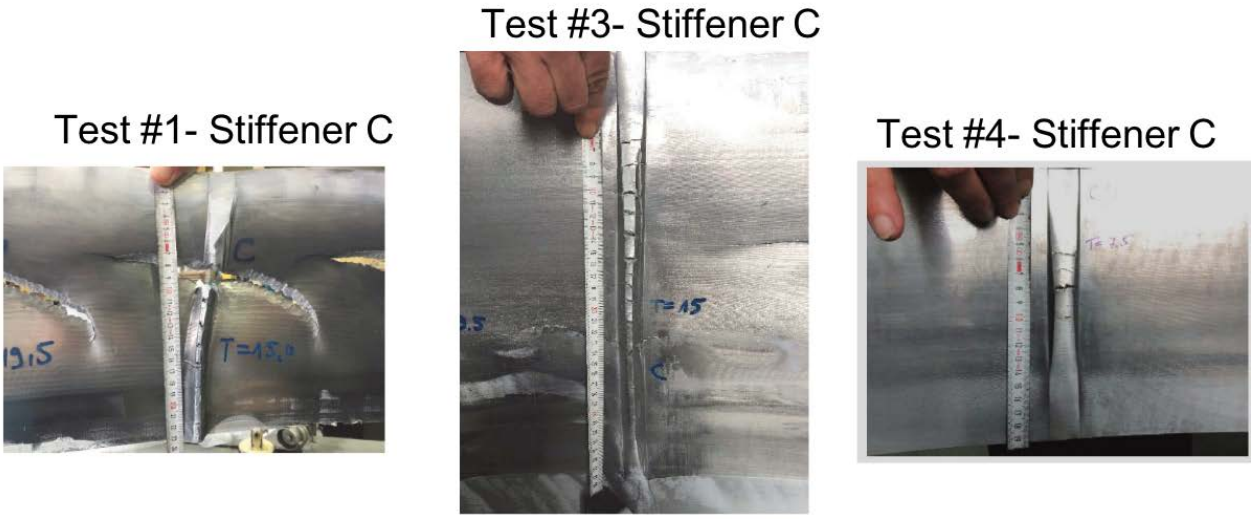

Figure 6. IML views providing comparison of stiffener C in tests #1, 3, and 4.

Arc segments containing stiffeners A-C and G-I from tests 3 and 4 were provided to NASA LaRC for analysis. Metallurgical cross-sections were extracted from test #3 with focus on stiffener letters A-C. These three stiffeners feature the same symmetric groove design. The only difference in the geometry of these three stiffeners is the depth of the groove on the mandrel. Stiffener C – the shallowest depth – repeatedly exhibited the best fill and least cracking of the three. A cut plan for metallurgical analysis is shown in Figure 7 denoted by the black boxes. Cross-sections through the stiffeners were taken from regions selected to minimize the amount of cracking encountered to better understand material flow and grain evolution in the best formed regions. In stiffeners A-C, the steady-state regions were analyzed to compare the effect of groove depth on flow features and formability. In stiffener C, regions from the start (top of panel) and end (bottom of panel) of forming were also examined to evaluate how material flow progresses during forming. Finally, a region from the base of the panel under stiffener C was examined to document the starting microstructure.

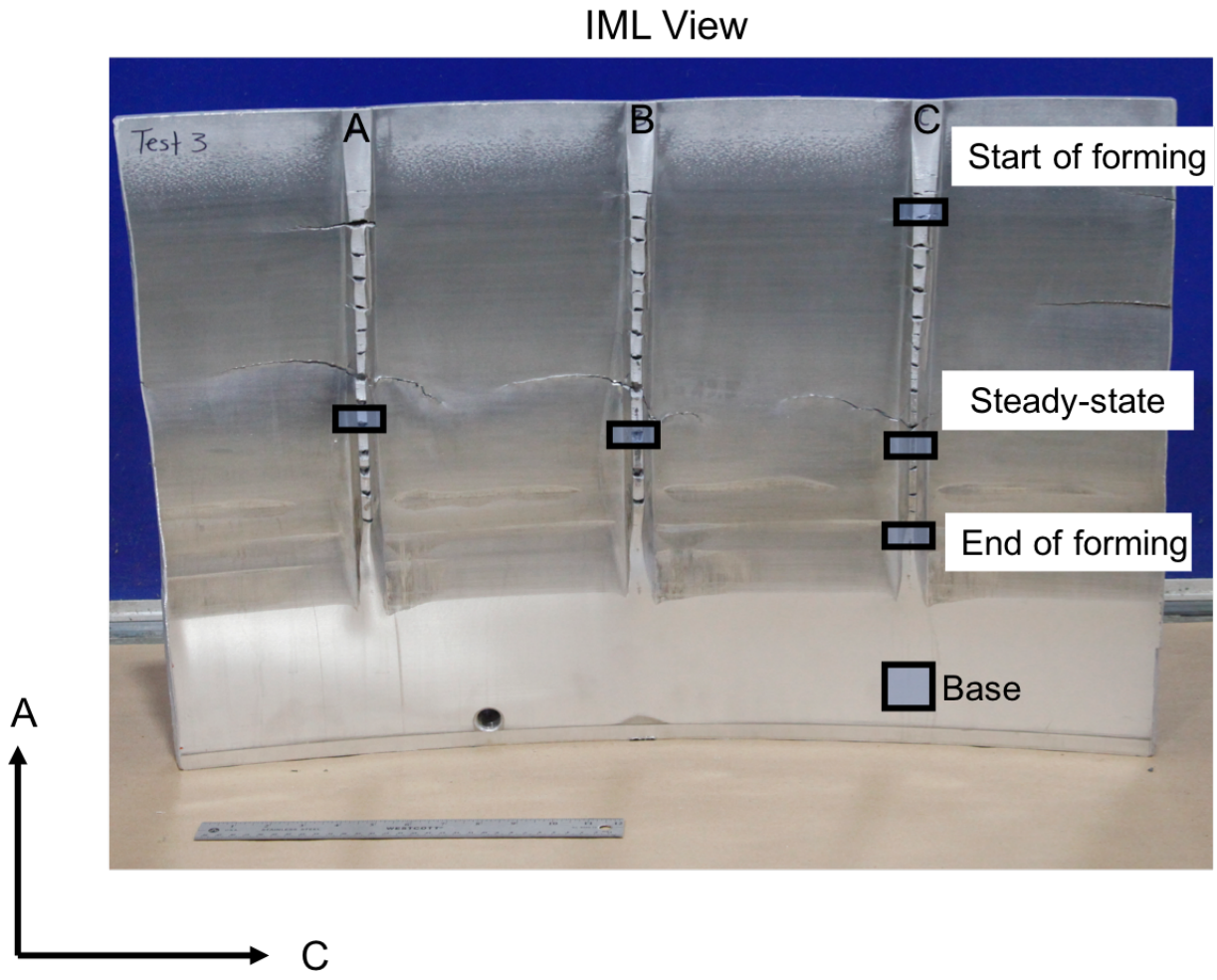

Figure 7. Cut plan for metallographic analysis of 10-ft. ISC segment from test #3 containing stiffeners A-C.

3. Experimental Procedures

3.1. Metallurgical Sample Preparation

Macro photographs were taken on as-received material. No mechanical polishing or grinding was performed. To reveal the grain structure, an etchant consisting of a ratio 10 ml H_2O to 1 g NaOH was used. Samples were immersed in this solution for 10 minutes and rinsed in a strong HNO_3 solution to clean off any surface contamination.

Metallurgical sections were mechanically polished using successive grit SiC paper ranging from 600 - 1200 grit. This was followed by a final polish using a colloidal silica-based suspension. Following mechanical polishing, some samples were viewed in the as-polished state and others were etched with suitable reagents to reveal the underlying microstructure. Images were captured using optical and scanning electron microscopy (SEM).

3.2. Heat Treatment to Improve Formability

Exploratory heat treatments were investigated to improve material formability in response to cracking issues encountered during forming. Segments from test #4 were used for preliminary screening of several heat treatment options as indicated in Figure 8. Test #4 experienced minimal forming and should be representative of the starting O-temper preform condition. Per recommendation of the preform ring manufacturer, Scot Forge, heat treatments that include slower cooling rates from the solution heat treat temperature (995 °F for Al 2219) can improve formability in aluminum alloys. This heat treatment is a variation of an O-temper anneal known as the O1 temper.

The O1 temper (previously referred to as the T411 temper) was initially developed to provide a more homogeneous microstructure for improved ultrasonic inspection signal [4]. However, it was also observed that this condition provided enhanced formability in some aluminum alloys, based on experiential knowledge from Scot Forge. Typically, O-temper annealing is done over the range 750 - 800 °F for Al 2219 (and other Al alloys) [4]. The O1 temper is performed at the higher solutionizing temperature and aims to revert as much solute as possible from second phase particles back into solid solution. The slow cooling is desirable to increase interparticle spacing by suppressing reprecipitation of smaller strengthening phases. This heat treatment study was performed to determine whether O1-type tempers produce enhanced formability in Al 2219.

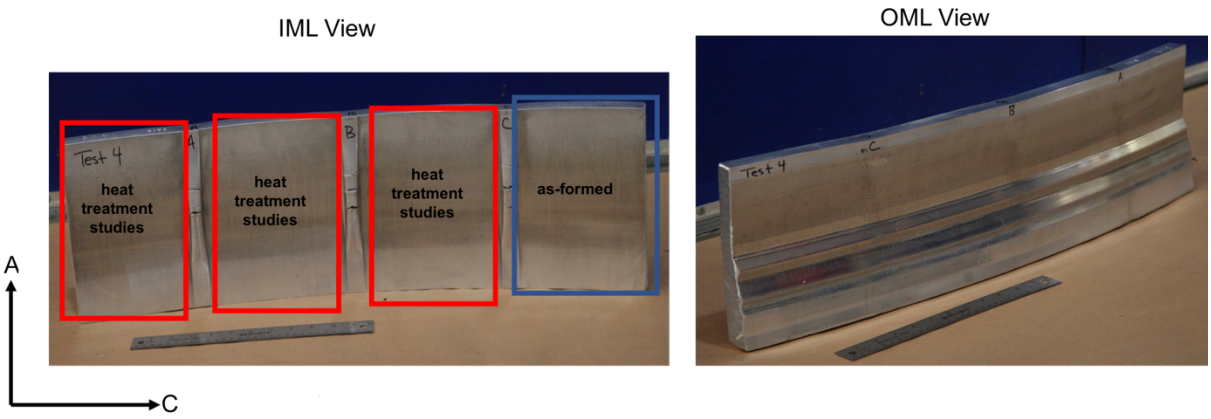

Figure 8. Test #4 (Al 2219) material used for preliminary heat treatment and metallurgical analysis.

3.3. Mechanical Testing to Evaluate Formability

Tensile test specimens were cut via wire electrical discharge machining (EDM) from base and wall locations and tested to evaluate formability. The as-formed base region segment was used to compare the formability in the starting O-temper condition versus the O1-temper heat treatment segments designed to increase formability. Base material was also compared to the specimens taken from the wall region in the as-formed state to evaluate the residual ductility before and after forming. The specimen layout is shown below in Figure 9. The specimens were cut in the axial and circumferential orientations of the preform rings. A specimen drawing is shown below in Figure 10 and conforms to sub-size specimen standards in ASTM E8 [5].

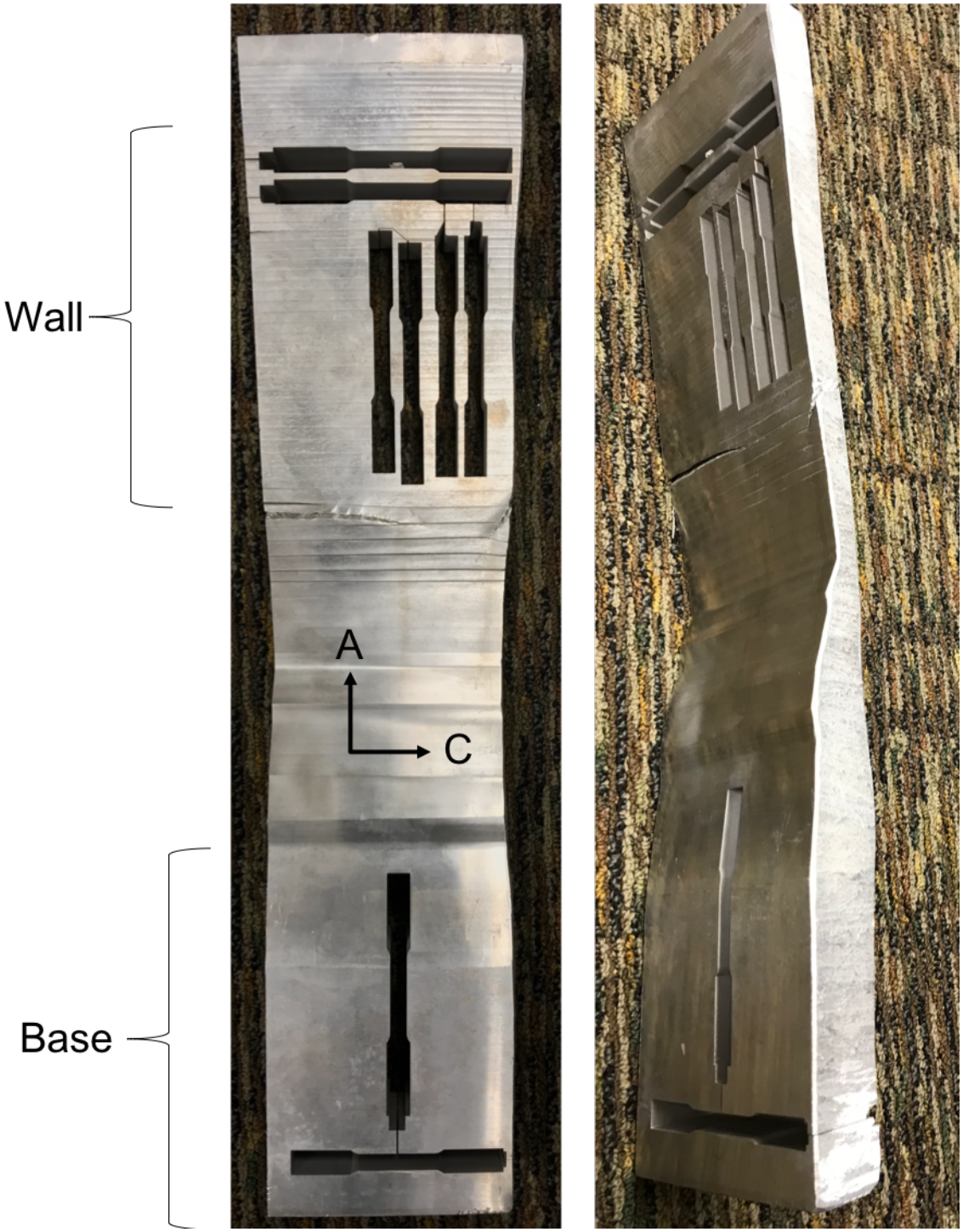

Figure 9. Tensile test specimen layout for Base (B3) and Wall (W3) from ISC #3.

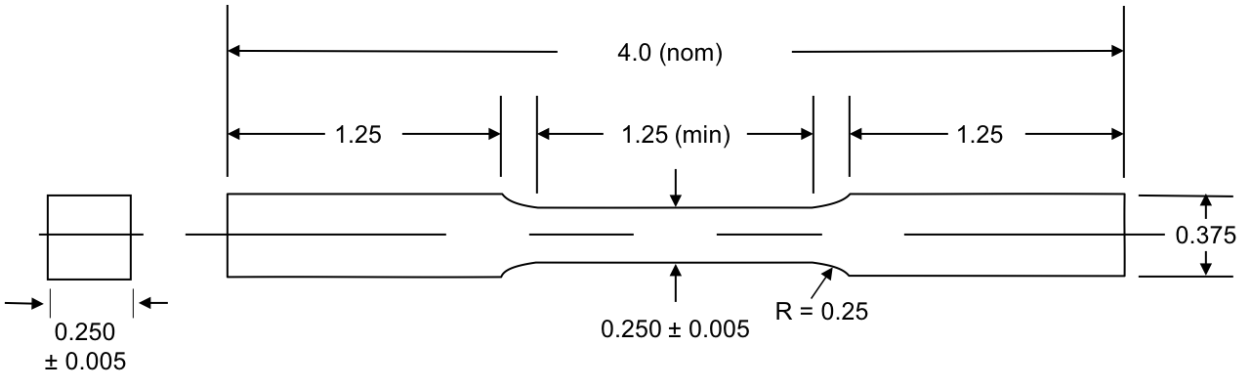

Figure 10. Tensile test specimen geometry and dimensions (inches).

A constant stroke rate of 0.01 in/min was used for testing. Digital image correlation (DIC) was used to compute surface strains from measured displacements within the gauge section. Four parameters were used to characterize material formability: 1) elongation at failure, 2) uniform elongation (defined as the elongation up to the ultimate tensile strength), 3) strain hardening exponent – n, and 4) plastic strain ratio – r. The latter two parameters are regularly used in the automotive industry to evaluate material formability for sheet applications, such as stamping or deep drawing.

The strain hardening exponent is derived from a power-law fit of the plastic portion of the true stress-strain curve between data bound by the yield (0.2 % offset) and ultimate tensile stress points as identified on the engineering stress-strain curve [6, 7]. The power-law fit in equation 1 assumes the following stress-strain relationship,

$$\sigma = K \cdot \varepsilon^{n} \qquad \text{(Eq. 1)}$$

where σ represents the true stress, ε represents the true strain, K is a fitting constant and n is the strain hardening exponent. ASTM test standard E646 [8] provides guidance on testing and analysis methods to compute the strain hardening exponent in metallic materials.

The plastic strain ratio equation 2 is defined simply as the ratio of the width strain to thickness strain,

$$r = \frac{\varepsilon_w}{\varepsilon_t} \qquad \text{(Eq. 2)}$$

where r is the plastic strain ratio, ε_w is the width strain and ε_t is the thickness strain (true strain is to be used for Eq. 2). ASTM test standard E517 [9] provides guidance on testing and analysis methods to compute the plastic strain ratio in metallic materials. It is customary that the through-thickness strain is not directly measured but recovered from an assumption of constant volume during deformation. The plastic strain ratio (also referred to as Lankford coefficient, or R-ratio) is a metric to evaluate formability anisotropy in different directions [10, 11]. The closer the R-ratio is to 1, the more isotropic the material is. Values far less than or greater than unity indicate anisotropy, and generally reduced formability due to a greater propensity for localization. In this study, there are two specific tensile test orientations: axial and circumferential. For the axial tensile specimens, the ratio is the measure of circumferential (width) to radial (thickness) strains. For the circumferential tensile specimens, the ratio is the measure of axial (width) to radial (thickness) strains.

4. Results

Initial inspection of the 10-ft. diameter as-formed segments revealed cracking in and around stiffeners. The focus of this materials characterization study is on stiffeners A-C from test #3, which have the same general geometry but different depths. The targeted depth of A was 1-inch; B was 0.75-inch; and C was 0.6-inch. Stiffener C was determined to have the best fill and least cracking of the three when examining both OML and IML surfaces. Images of the OML and IML surfaces are shown in Figure 11. All cracking observed appears to originate within the stiffeners. Most of the cracking is confined within the stiffeners but there are several occasions where the cracking propagates into the wall section due to continued forming after the onset of cracking within the stiffeners. This suggests that failure is occurring due to issues with stiffener fabrication and not with respect to flow forming of the wall.

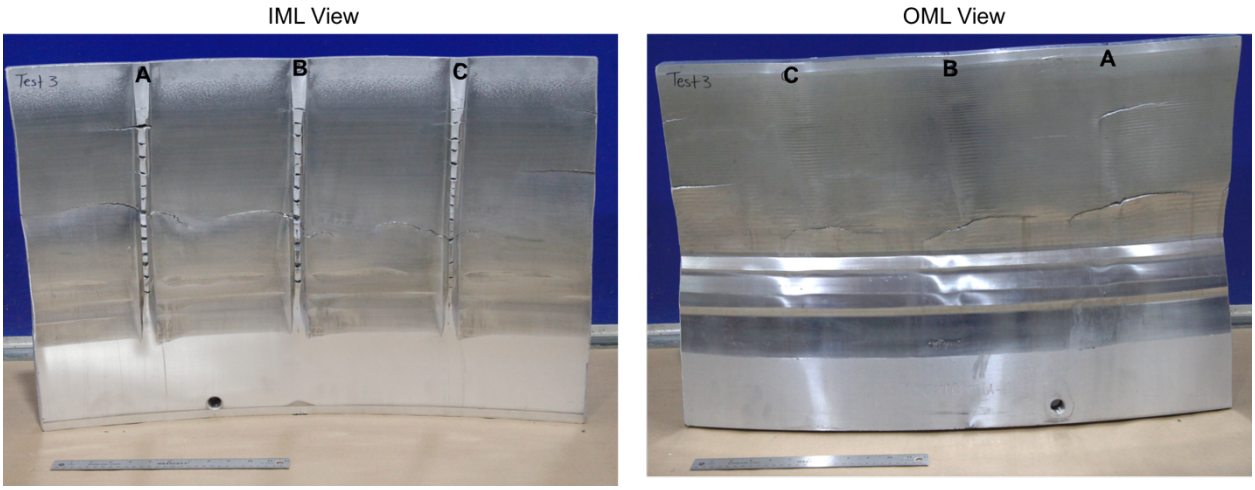

Figure 11. IML and OML views on Al 2219 test 3 segment with stiffeners A-C.

One possible cause of cracking is differential material flow rates between the wall and stiffener during axial growth of the cylinder. A view of the OML surface and associated cracking is shown in Figure 12. The location of the stiffeners on the IML surface correspond to the periodically spaced defects oriented in the axial direction of the ISC part. The hypothesis of differential material flow rates between the wall and stiffener regions is supported by the observed scalloping on the top surface of the ISC, highlighted in Figure 12. Scalloping suggests that the flow rate in the axial direction in the wall, $\dot{m}_{\text{axial},2}$ is greater than the axial flow rate in the stiffener, $\dot{m}_{\text{axial},1}$. This is rationalized by considering the increased material flow rate in the radial direction within the stiffeners, $\dot{m}_{\text{rad}}$, requiring increased mass consumption in the stiffener compared to the wall and thereby decreasing the stiffener axial flow rate. The differential flow will lead to development of tensile stresses in the axial direction in the stiffeners and may explain the cracks that occur nominally perpendicular to the axial direction. The observation that the shallower grooves led to stiffeners with less cracking is attributed to the increased radial component of flow required for taller stiffeners. The larger $\dot{m}_{\text{rad}}$ for the taller stiffeners leads to a greater difference in axial flow rate between the wall and stiffener.

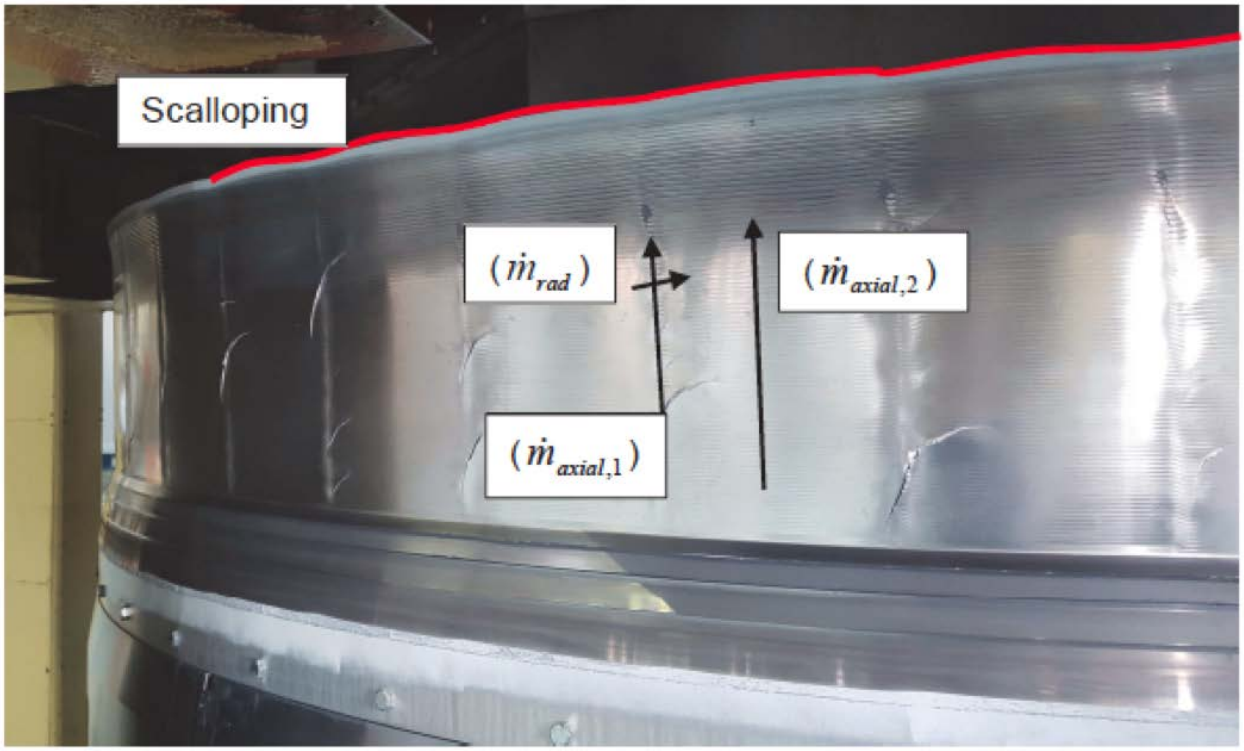

Figure 12. Evidence of scalloping on top surface and depiction of differential material flow rates between wall and stiffener. (Image used with permission from MT Aerospace)

4.1. Metallurgical Evaluation of As-Formed Material

Macro photographs of stiffener A from test #3 and the adjacent IML wall surface were captured before and after etching to provide a global assessment of cracking in relation to grain structure. These images are shown side by side in Figure 13. A fine-grained microstructure is revealed after etching and the cracking does not appear to follow any features on the grain structure along the IML surface and external edges of the stiffener. A fine-grained microstructure is beneficial for improved formability and these images verify that the preform rings were produced with a desirable grain structure. The top of the image corresponds to the top of stiffener, where forming started and the stiffener began to fill. Note that cracking within the stiffener occurs early in the process as the stiffener starts to form. Numerous smaller cracks are visible in the stiffener that are not easily distinguishable in the image. Cracking appears to originate within the stiffener and in some instances spread into the wall of the cylinder to form longer cracks. Cracking in the wall is attributed to continued forming after the first audible indications of cracking during the ISC process.

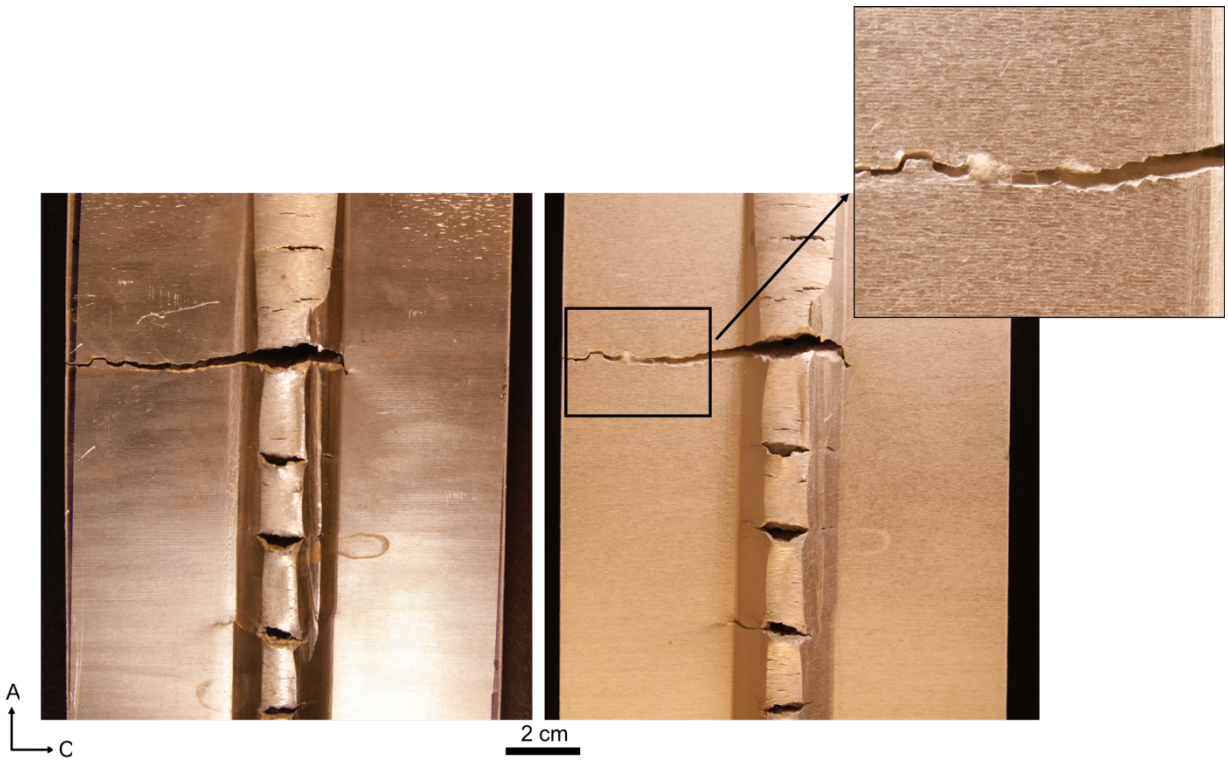

Figure 13. Macro photos of stiffener A (IML view) from test #3 before (left) and after etch (right) with zoomed in region (upper right) to better show grain structure.

Further examination of the microstructure in the starting material was performed using optical microscopy. Metallurgical cross-sections from the three principal planes in the cylinder (A-R, R-C, and A-C) are shown in Figure 14. The images reveal an elongated grain structure in the circumferential direction, which is expected for a ring rolled product. In the other two directions, the grain thicknesses in the axial and radial directions are comparable. To this point, the grain structure in the A-R plane is a roughly equiaxed microstructure. Two features stand out in these images. First, there are chains of large particles (sometimes commonly referred to as stringer particles) in the A-C and R-C planes. Several examples of stringer particles are highlighted in those images. These particles are generally aligned in the circumferential direction. Second, the grain structure in the A-R cross-section is slightly elongated at 45° within that plane. This indicates that the microstructure is canted to both the axial and radial directions. This is not typical for more common products forms, such as rolled plate or sheet material, and may be unique to ring rolled microstructures.

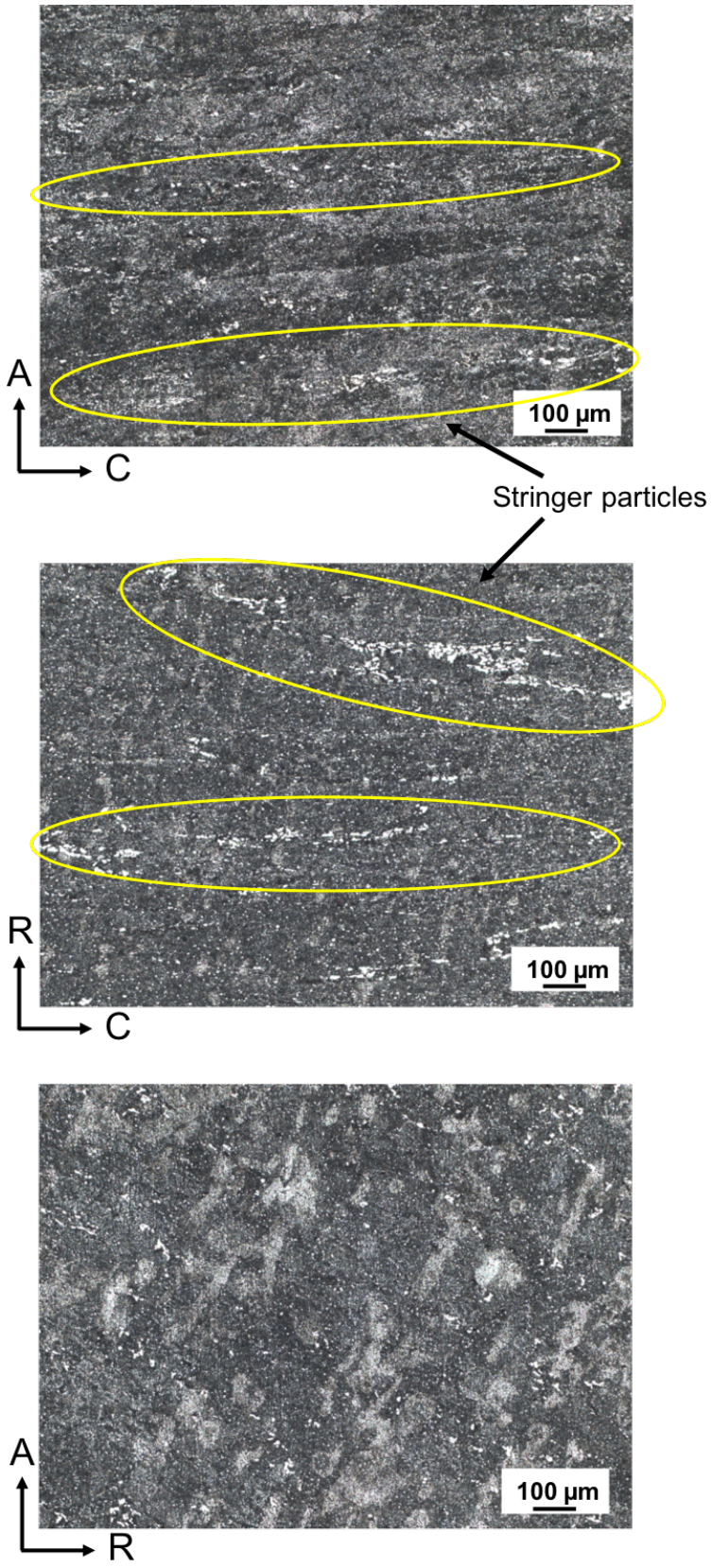

Figure 14. Photos from each of the three orthogonal planes, (top) A-C, (middle) R-C, and (bottom) A-R, from the base region in ISC test #3.

A series of three metallurgical cross-sections were prepared from the test #3 stiffener C, in the as-formed condition as shown in Figure 15. All were etched with Keller's reagent to reveal the microstructure. The three locations selected are notionally labeled in Figure 7 and correspond to the start of forming (top of ISC), steady state region (middle of ISC), and the end of forming (bottom of ISC). The steady state region allows assessment of material flow and quality of the fill in a region where maximum fill is expected and the process has theoretically reached the most uniform forming condition. Examination of the start and end of forming in regions of partial stiffener fill provides a glimpse at how the fill evolves during the process.

At the start of forming, the material flow patterns appear largely symmetric about the centerline of the stiffener as material is initially flowing radially into the groove (upward in the images). There is a noticeable stairstep along the downstream side (left hand side) of the stiffener. A slight asymmetry in material flow that becomes more noticeable as the stiffener fills leads to the upstream side (right hand side) filling slightly ahead of the downstream side of the stiffener. Consequently, friction and non-continuous material flow along the groove in the mandrel on downstream side likely caused this feature. Friction effects will be discussed in more detail in succeeding paragraphs. In the steady state section, the flow is significantly more asymmetric about the centerline of the stiffener. Some indications of poorer flow along the downstream side of the stiffener are observed, leading to an outer edge of the stiffener that is not as linear as the upstream side (right side of image). At the end of forming, the flow lines are slightly less symmetric than at the start of forming, but considerably more symmetric than the steady state region. This indicates that the asymmetry increases with increasing stiffener fill. This is attributed the circumferential component of material flow that is increased with multiple roller passes due to the part spinning during the process. There is also a small indication of a stairstep along the downstream side of the stiffener at the end of forming, attributed to frictional effects during processing.

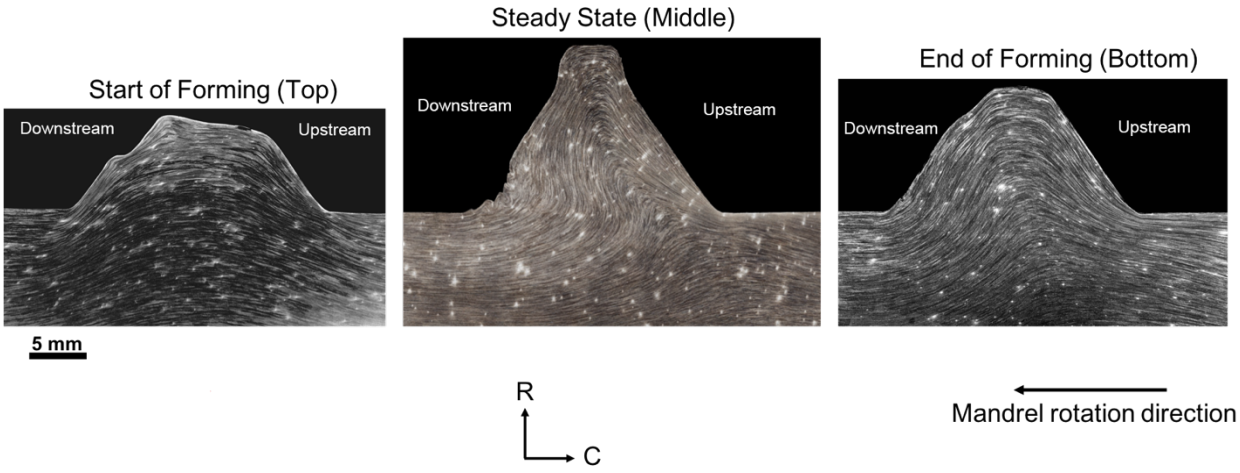

Figure 15. Metallurgical cross-sections from test #3 stiffener C at the start, steady state, and end of forming.

Stiffener cross-sections from the steady state regions of A-C from test #3 are shown in Figure 16. These cross-sections were intentionally selected from regions with no visual surface indication of cracking to evaluate regions of best forming within each stiffener. These samples were etched with Keller's reagent to reveal grain boundaries, providing indications of material flow in the stiffener. Material flow in all three stiffeners was similar, revealing asymmetric material flow lines about the centerline of the stiffener. The asymmetry was developed from a circumferential component of material flow due the rotational nature of the process, leading to the upstream side filling ahead of the downstream side. Compressed flow lines on the upstream side of the stiffener

(right hand side) are indications of higher stresses acting normal to the surface of the groove than on the downstream side, where the flow lines are more widely spaced. Cracking was observed in the center of the cross-sections of stiffeners A and B, while no cracking was found in stiffener C at 25x magnification. However, there was evidence of small notch-like defects along the downstream side of stiffener C. The internal cracking in A and B appears to follow (to some degree) the flow path in the center of the stiffener. This suggests there is an impact of the local microstructure and/or material flow on the cracking behavior. Stiffeners B and C reached complete fill of the groove; B reached a height of 0.8 inches and C reached a height of 0.6 inches. Stiffener A reached a height of 0.8-inch, less than the desired fill of 1 inch. This does not indicate a limit in stiffener fill for the process as 1-inch tall stiffeners have been achieved in smaller diameter forming trials during ISC development, but may reflect having stopped the ISC process due to audible evidence of cracking before groove A could be completely filled.

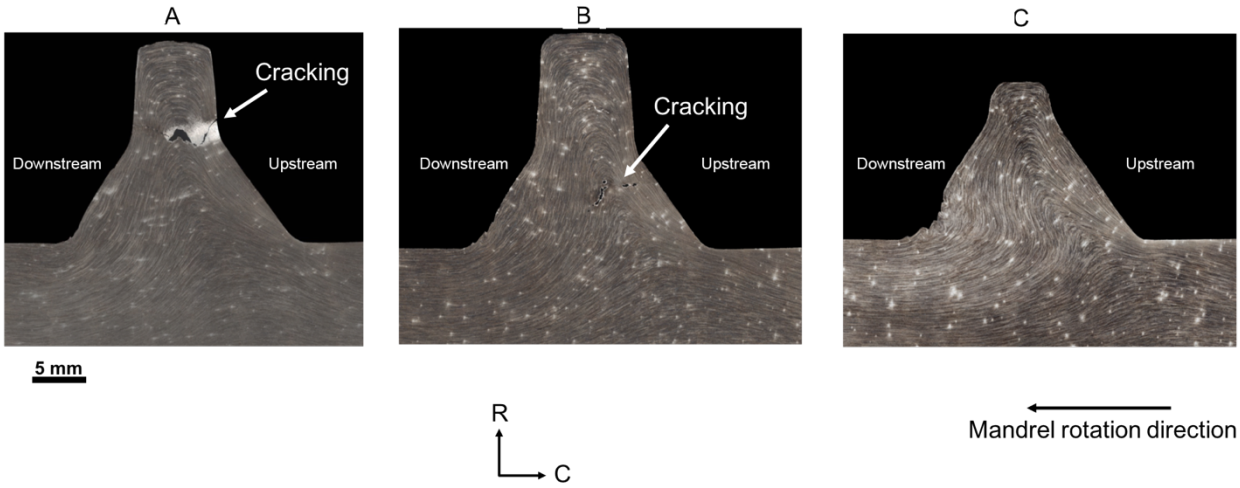

Figure 16. Metallurgical cross-sections of stiffeners A-C steady state region from test #3.

In Figure 16, evidence of cracking was observed in stiffeners A and B that appeared to correlate with flow lines within the stiffener. Further examination of these regions at higher magnification in the SEM found correlation with a high incidence of larger particle cracking or separation from the matrix in regions surrounding the cracks. In the image for stiffener C taken at 25x in Figure 16, there were no cracks evident in those same areas. Upon further investigation, smaller cracks were found that appear to follow flow lines similar to those observed in stiffeners A and B. The presumption is that these smaller cracks may provide insight into the formation of the larger cracks. Two subsequently higher magnification regions along those cracks are shown in the bottom row of Figure 17. There is a correlation with crack location and position of large, constituent particles, indicating that cracking likely originates at these large particles and propagates along neighboring particles. Particles most prevalently observed with cracks or adjacent to cracks are larger in size with faceted shapes (non-circular edges). It is assumed that cracking is most apparent in the region where the flow pattern shows an inflection point because this is likely a region of high strain. High strains are created as the material is pushed into the groove and the grains are required to bend, giving rise to a small radius of curvature in these regions.

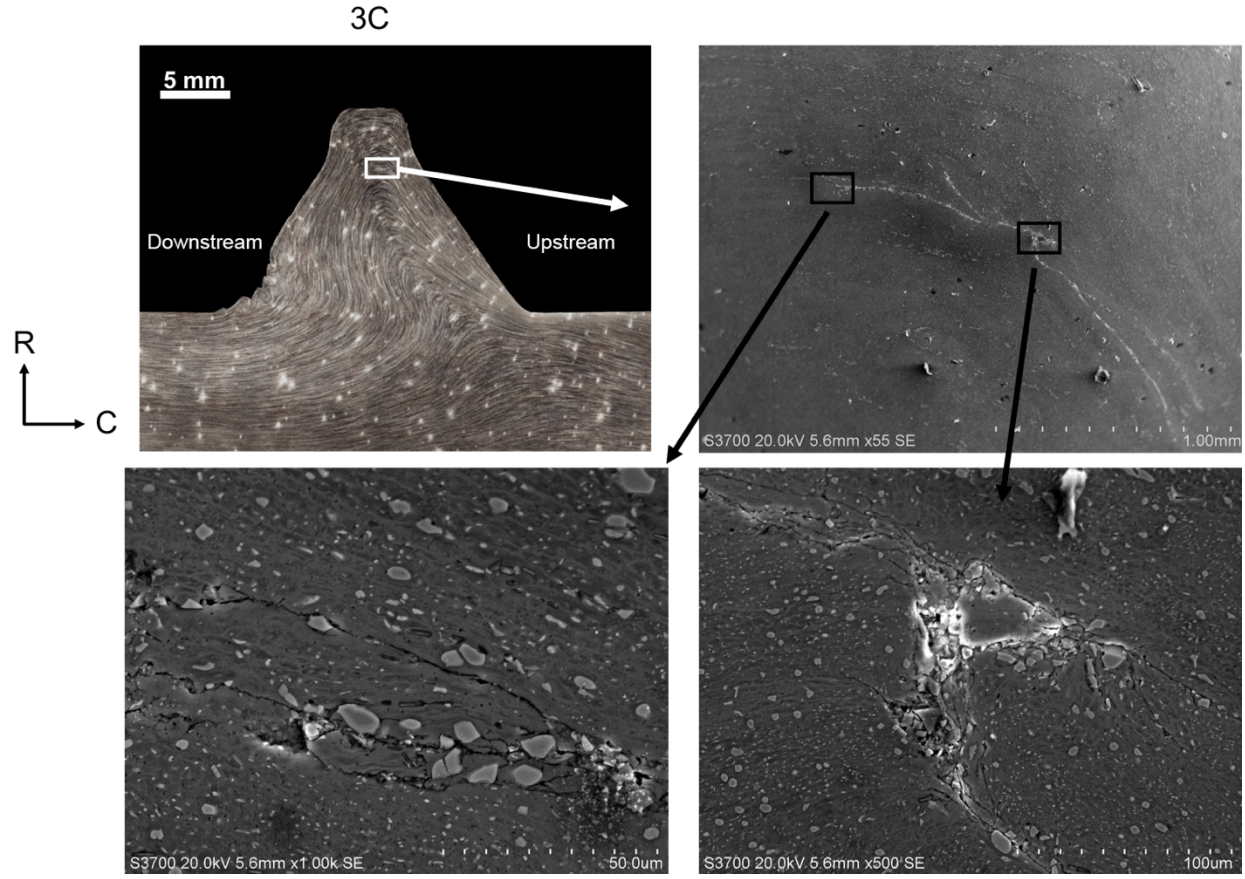

Figure 17. Higher magnification images of small cracks in stiffener C from test #3.

In addition to some cracking in the middle of the stiffener, small cracks were observed at notches seen on the downstream surface of the stiffener just above the wall. These notches correlated with marks on the outside of stiffener C on the downstream side as seen in Figure 18. The marks tend to be more numerous at the start of forming, and persist down the entire length of the stiffener. Discussions with Scot Forge suggested that these marks are indications of stick-slip friction during the ISC process, leading to the striations observed along the outer surface of the stiffener, and subsurface notches seen within the stiffener cross-sections. These parallel striations occur as metal repeatedly sticks and tears as it slides across the mandrel surface during forming. Stick-slip friction is attributed to improper lubrication. MT Aerospace used the standard lubricant for booster fabrication during the 10-ft. diameter ISC forming campaign. Consultation with tribology and lubrication experts determined that this lubricant is better suited for hot-working applications (forging, extrusion, etc.) rather than ambient temperature metal forming. Those experts recommended a different lubricant, which is formulated for warm to hot forming of dies with shallow cavities or ribs, much like the ISC process. Based on this input, NASA and MT Aerospace are working with a lubricant manufacturer to identify the most suitable lubricant for ISC forming.

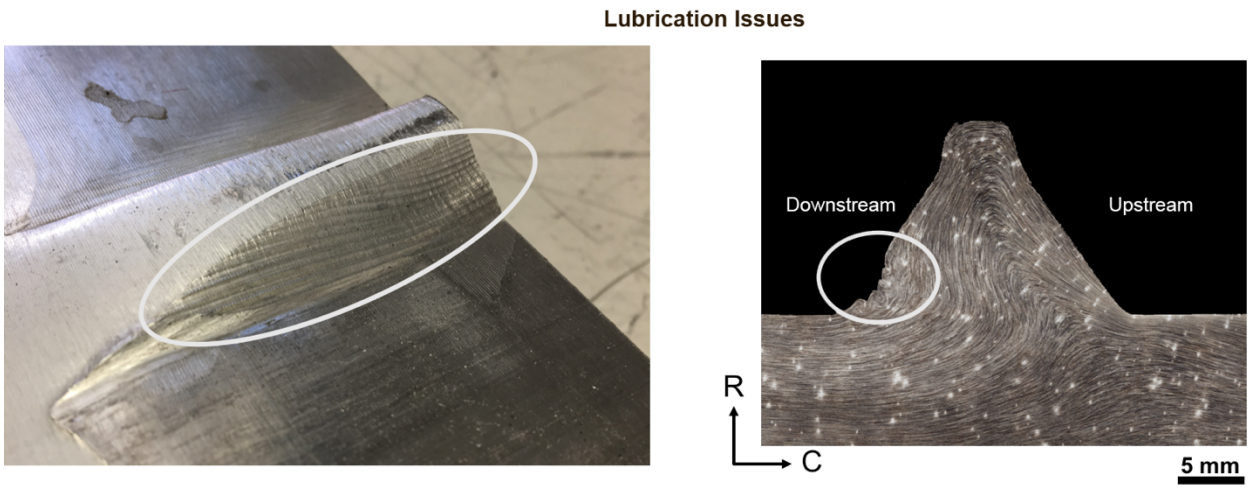

Figure 18. Evidence of stick-slip friction due to lubrication issues on downstream side (left hand side) of stiffener C from test #3.

A series of higher magnification images of the notches in stiffener C are shown Figure 19.The images reveal three subsurface cracks along the outer edge of the downstream side of stiffener C. This side is slower to fill, leading to the asymmetry of the material flow into the stiffener. As a result, this side is anticipated to see higher frictional stresses than the opposing upstream side of the stiffener. There is some similarity of these notches with the stairstep features noted at the start and end of forming in Figure 15. One possible explanation is that these notches originate due to repeated sticking and slipping during the fill of the stiffeners, which may give rise to the irregular flow patterns around the notches. A stitched set of higher magnification images of one of the subsurface cracks shows the path tends to follow coarse stringer particles. No such notches or subsurface cracking was found on the upstream side of the stiffener. Thus, surface lubrication issues led to higher stress concentrations on the downstream side of the stiffener. As a result, cracking initiated along the surface and continued to propagate along chains of large particles to depths of several hundred micrometers into the stiffener. It is anticipated that similar mechanisms result in the large cracks observed elsewhere in the stiffener.

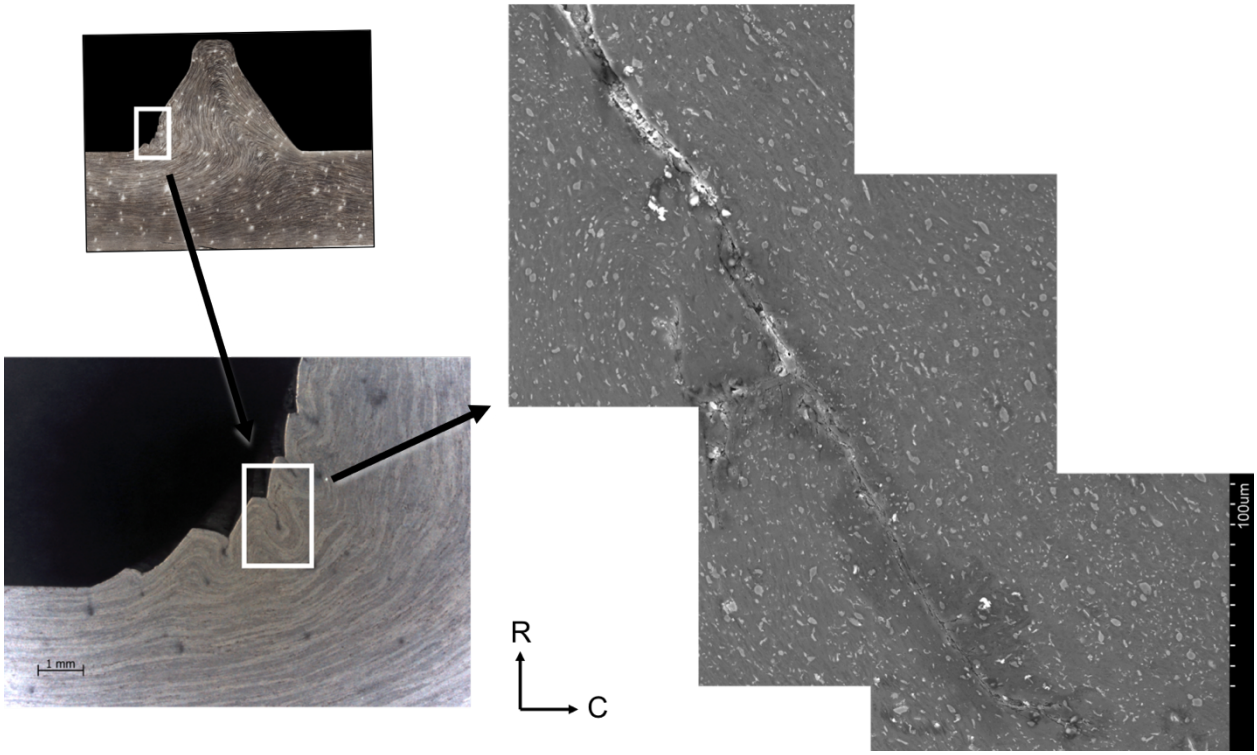

Figure 19. Higher magnification images of cracks along downstream (left hand) side of stiffener C from test #3.

A high magnification optical image from the wall region directly below stiffener C in test #3 is shown in Figure 20. Large Al_2Cu particles ranging in size up to ~ 50 µm were observed. A crack was found to have propagated along some of the large particles highlighted with arrows, via apparent cracking along multiple particle-matrix interfaces. With numerous large particles arrayed throughout the stiffener, it is likely that multiple micro-cracks may form at these particles and link together, which serves as a mechanism for some of the larger cracks observed in test #3. In conjunction with the extent of cracking associated with particles in the stiffener region and below the stiffeners, these images highlight the occurrence of higher stresses locally in and around the stiffener region associated with forcing material to fill the grooves.

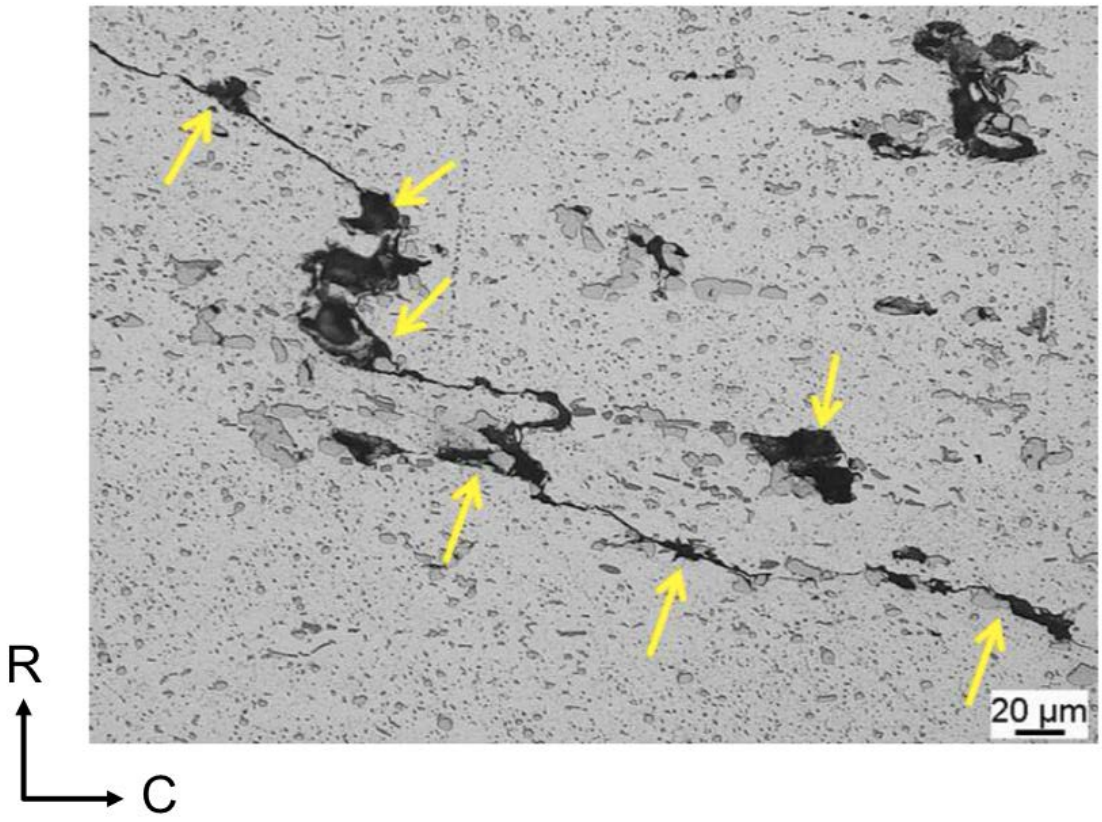

Figure 20. Additional evidence of cracking along particles (highlighted by arrows) from the wall region beneath the stiffener.

Further examination with optical microscopy was conducted on a similar polished cross-section from the wall region (remote from the stiffeners) of test #3 as shown in Figure 21. Within the wall, several of the larger particles exhibit small cracks along their edges. However, the extent of cracking was far lower than regions near the stiffeners. In addition, the cracks around particles did not link up to form larger cracks as was observed in regions near the stiffeners (Figures 17 and 20). This suggests that significantly higher stresses are occurring within the stiffeners compared to the wall during forming, as the extent of crack nucleation and coalescence along these stringer particles in the stiffeners would require higher stresses. The extent of the role that friction plays in this behavior is unclear. However, increased friction will only lead to higher stresses during forming and hence a greater propensity for cracking. Thus, attempts to reduce friction will be beneficial to the success of the ISC process.

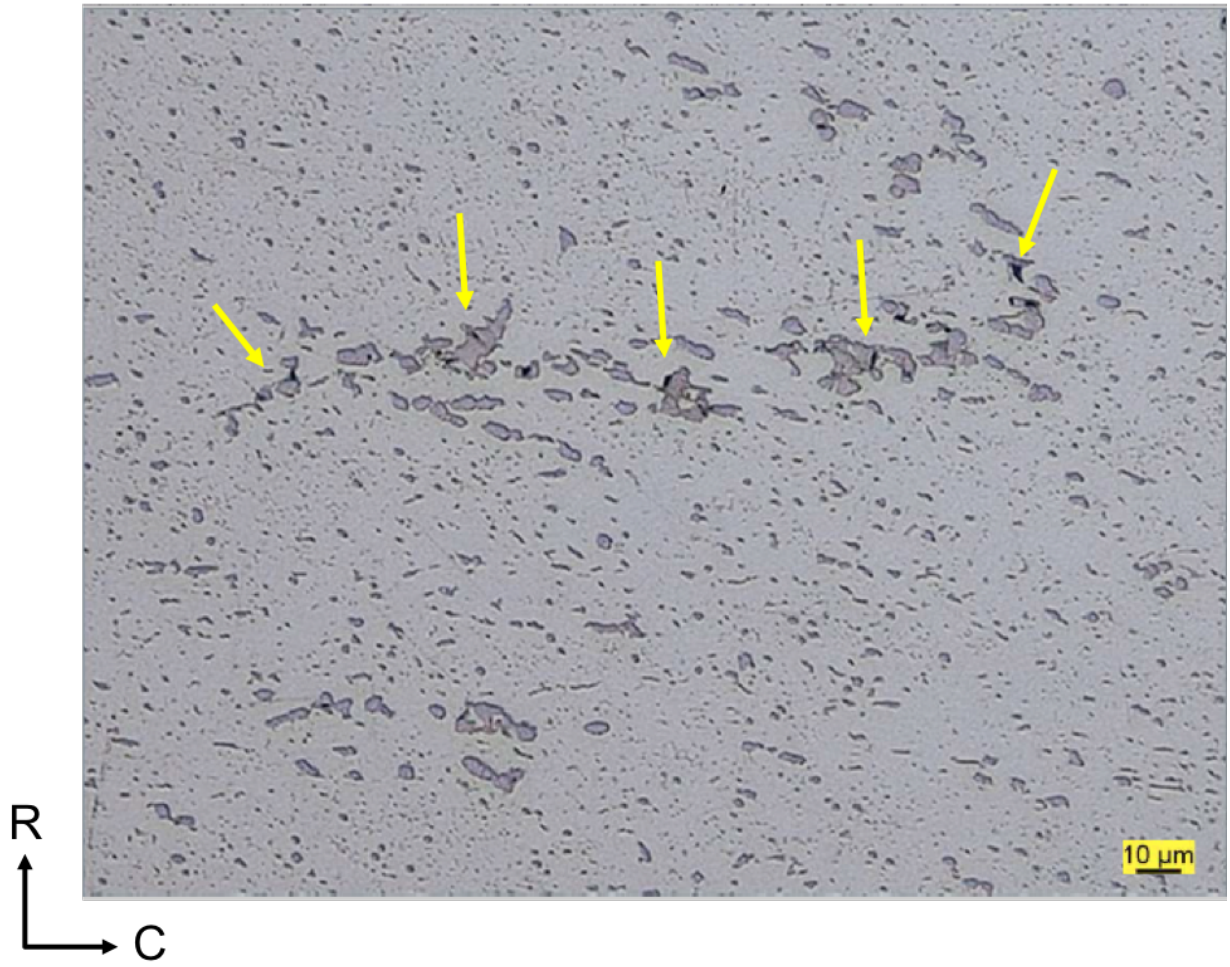

Figure 21. Evidence of cracking near particles (highlighted by arrows) in the wall region remote from stiffeners.

Finally, a polished cross-section from the unformed base region of test #3 was photographed using optical microscopy and is presented in Figure 22. In this image, none of the particles exhibit any signs of cracking. This confirms that the starting preform rings were provided without existing damage around particles and that the cracking results purely from the applied mechanical stresses associated with the ISC forming process.

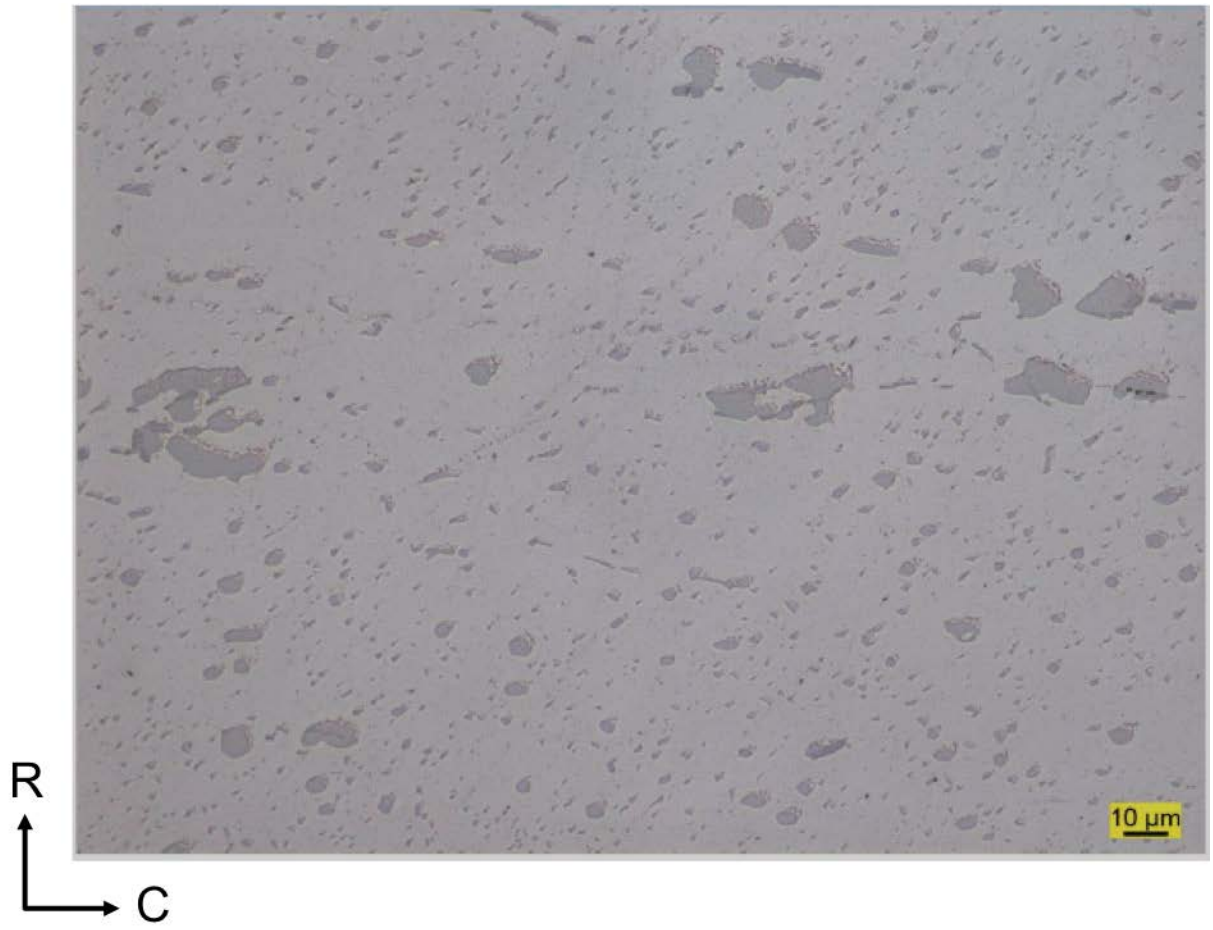

Figure 22. No apparent cracks in or around particles in the stating material from the unformed base.

4.2. Experimental Heat Treatments to Improve Formability

Table 2 summarizes the conditions evaluated and heat treatment parameters for Al 2219 material extracted from test #4. A portion of the material was evaluated in the as-formed condition, which had experienced minimal forming. This material nominally represents the starting ring condition, which was in an annealed, O-temper state. This serves as the starting condition for the other three heat treatment conditions. Two additional pieces from test #4 were given O1 temper heat treatments. Both O1 temper heat treatments, referred to as HT1 and HT2, were held at the solution heat treat temperature of 995 °F for 2 h, but were subjected to different cooling rates. An additional heat treatment was performed which is a typical pre-forming anneal used in MT Aerospace's commercial practice for Al 2219. It is designated as the "MT" condition and essentially is a variation of the AMS specification 2770 [4] with a slightly higher cooling rate.

Table 2. Description of sample conditions and heat treatment parameters.

Designation	Heat Treatment Description
AF	As formed condition; Nominally unformed region from base of ISC test #4. Ring was given O-temper anneal at 775 °F for 3.75 h during fabrication at Scot Forge and an uncontrolled air cool to room temperature. This is the starting condition for the other three heat treatments.
HT1	Solution treat at 995 °F and hold for 2 h. Allow material to cool uncontrolled in the furnace to room temperature. 24 h total cooling time.
HT2	Solution treat at 995 °F and hold for 2 h. Controlled cool in furnace at a rate of 12 °F/h to room temperature. 72 h total cooling time.
MT	Anneal at 775 °F and hold for 2 h. Control furnace cool at 86 °F/h to 300 °F. Material removed from furnace and allow to air cool to room temperature. 5.5 h cooling time in furnace.

For HT1, the uncontrolled furnace cool resulted in a bi-linear slope for the cooling profile. Thermocouple data for this heat treatment is shown in Figure 23. The reason for the bi-linear behavior is that the furnace fan was required to remain on until approximately 400 °F to prevent damage to heating elements. Two dashed lines approximate the average cooling rate over the two regions. From 995 - 400 °F, the cooling rate on average is 162 °F/h, whereas once the fan was turned off, the cooling rate slowed to roughly 14 °F/h from 400 - 100 °F. The total cooling time from 995 to 100 °F was roughly 24 hours.

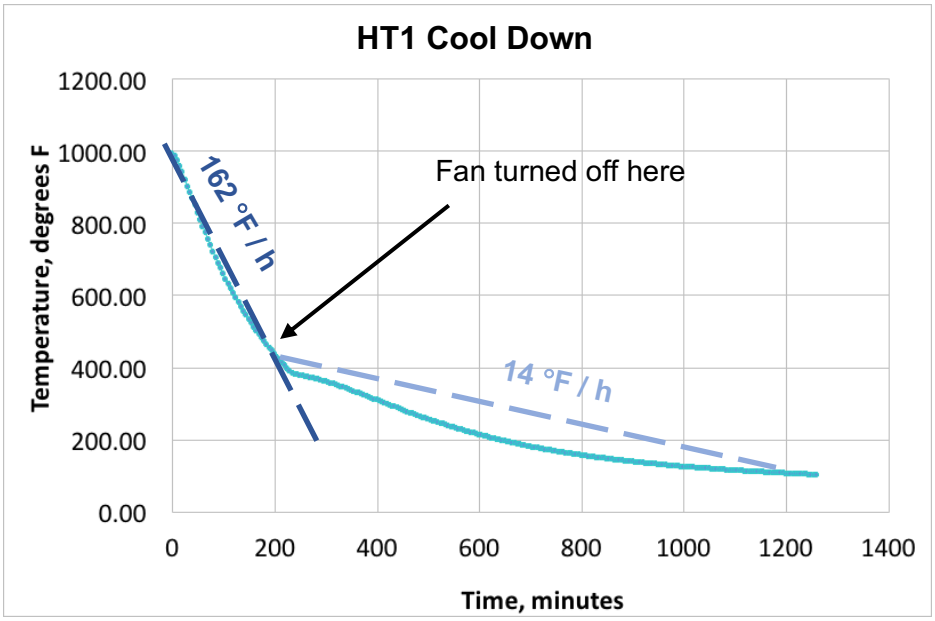

Figure 23. Cooling curve for HT1. Dashed lines approximate average cooling rates of regions before and after the fan was turned off.

For HT2, a controlled furnace cool was selected at a rate of 12 °F/h, which is roughly the same rate experienced once the fan was turned off for HT1. The cooling curve for this heat treatment is shown in Figure 24. The total cooling time was approximately 72 hours. The MT anneal was performed at 775 °F for 2 hours, followed by a controlled cool at 86 °F/h down to 300 °F as shown in Figure 24. The controlled cooling time was approximately 5.5 hours.

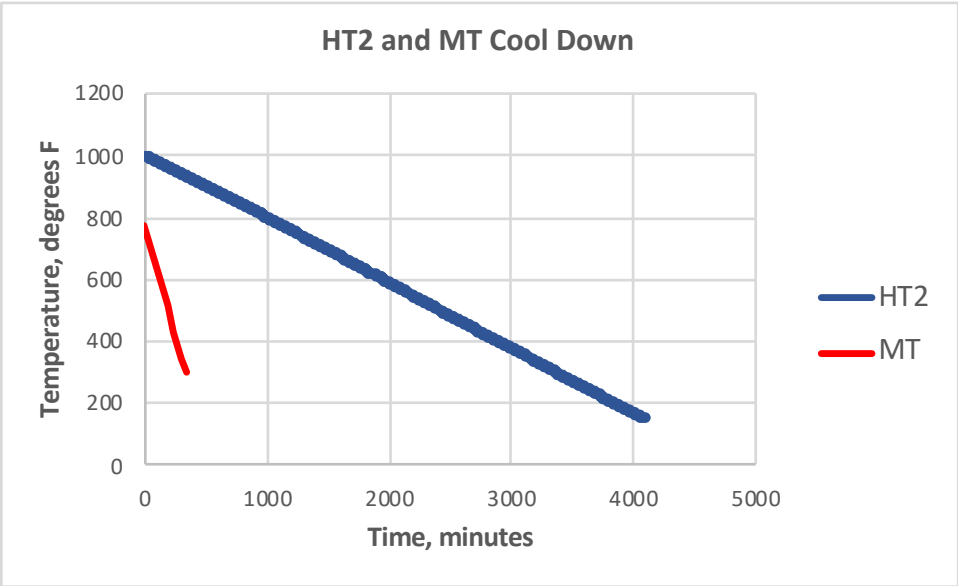

Figure 24. Cooling curve for HT2 and MT heat treatments.

4.3. Metallurgical Evaluation of Samples Heat Treated to Improve Formability

Scot Forge, the preform ring supplier, provided consultation to address material formability issues encountered in the 2017 ISC forming campaign. They provided suggestions for heat treatments that yielded improved formability in other Al alloys. The objective of the heat treatments was to increase particle spacing and provide a more uniform microstructure for enhanced formability. Preliminary assessment of the impact of the four heat treatments conditions noted in Table 2 was conducted using metallographic techniques. They also suggested mechanical testing to measure two parameters that gauge formability: 1) strain hardening exponent (n) and 2) R-ratio. These parameters are well-documented for their use in the automotive industry for sheet metal forming processes [6, 10-12].

Given the well-documented chemistry and microstructural information available for Al 2219, limited chemical analysis was performed to identify particle composition [13, 14]. Two conditions, AF and HT1, were evaluated as these should show the maximum difference in microstructure. As a result of the high Cu content in this alloy, one expects the majority of particles to contain Cu. A smaller fraction of particles also contains impurity elements, such as Si and/or Fe. This is indeed the case as revealed using energy dispersive spectroscopy (EDS) as seen in Figure 25. The large, Cu-rich particles are expected to be the equilibrium θ phase. The smaller phases may be either the metastable θ′ strengthening precipitate, which tends to have a high aspect ratio, or θ. The larger θ phase was identified to form between 752 and 887°F by combined differential scanning calorimetry (DSC) and transmission electron microscopy (TEM) analysis [14]. The θ′ phase was found to precipitate between 392 and 572 °F [14]. Both θ and θ′ have the same Al_2Cu stoichiometry.

In the AF condition, particles tend to be Cu-rich (primarily expected to be θ) along with some larger Fe-Al-(Si) intermetallic particles. This is expected to be similar to the particle composition in the MT condition, as both conditions are in an O-temper state. In HT1, the reduction in larger Cu-rich particles promotes the formation of numerous smaller Cu-rich phases, likely indicative of θ′.

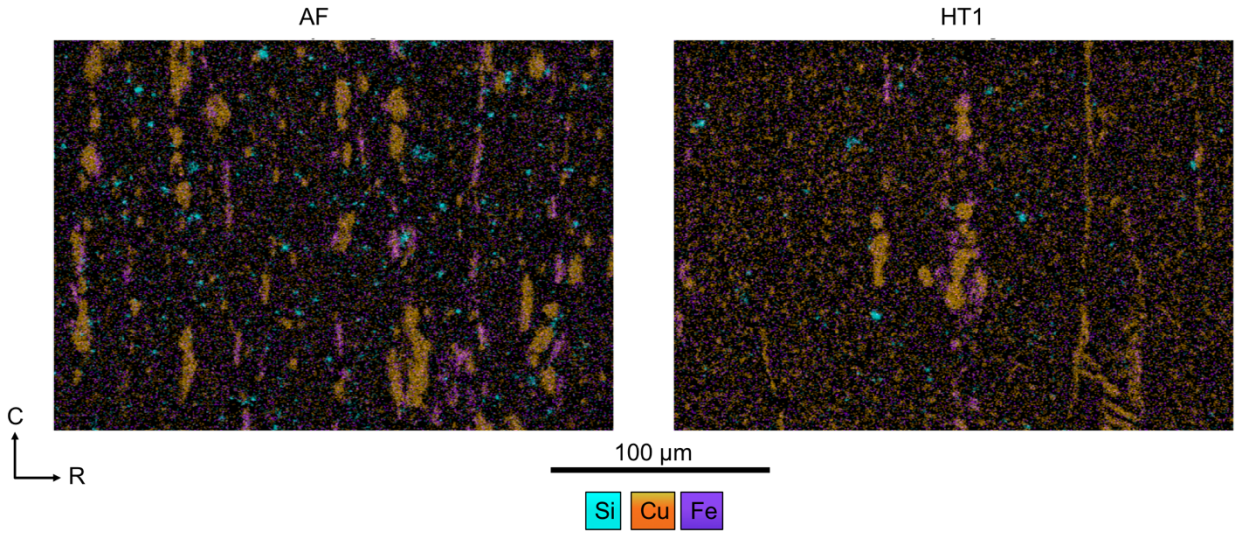

Figure 25. EDS elemental maps for the AF and HT1 conditions.

To characterize the effect of the heat treatments, images of the particle microstructures in the starting condition and heat-treated states were collected. This comparison is shown through low magnification scanning electron microscopy (SEM) images in Figure 26. Large-area, low magnification images enable qualitative assessment of the global distribution/variability in large particle size, shape, and spacing. It is difficult to assess similar features of smaller particles at this scale.

In the AF condition, particles range in size up to ~ 50 µm. Most particles tend to be oval or spherical in shape, likely the θ phase based on observations of an Al 2219-O condition reported in [14]. Some clustering is observed. Particles are generally aligned in the circumferential direction, which is the principal working direction for the ring rolled preforms. The AF and MT conditions look similar as one might expect, given that they are variants of the standard O-temper annealing practice. The MT heat treatment has a slightly faster cooling rate than the O-temper treatment applied to the preforms. However, there were no noticeable differences in particles size or distribution between the AF and MT conditions.

HT1 and HT2 resulted in more elongated particles with lengths occasionally in excess of 50 µm. This is likely the result of θ particle coarsening due to increasing the level of Cu in solution and subsequent precipitation during the extended slow cool period. The greatest difference compared to the AF condition occurs in HT2, which is the slowest cooling rate. In this condition, interparticle spacing is maximized and consequently particles are coarser as result. At low magnifications, HT1 looks similar to the AF and MT conditions.

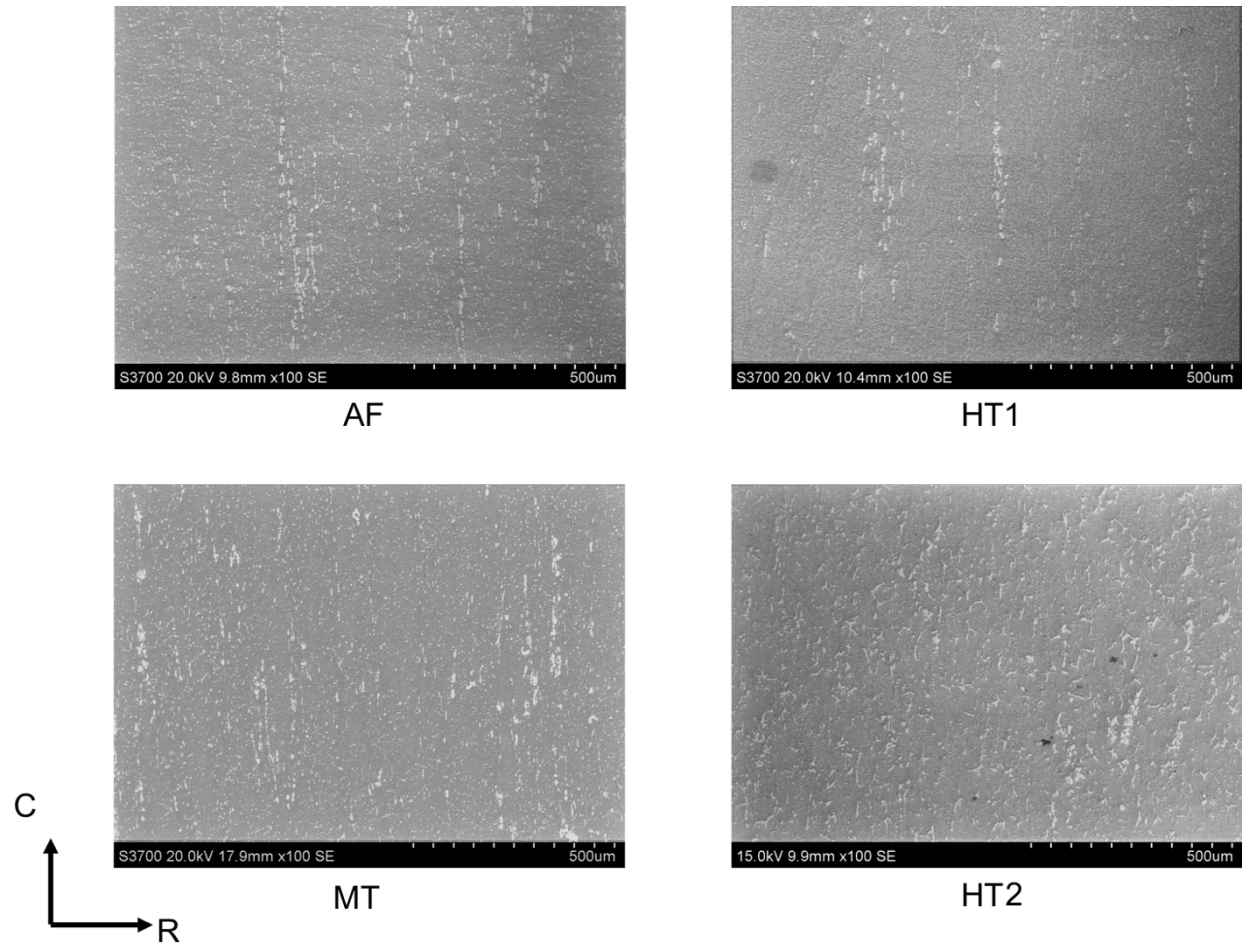

Figure 26. Low magnification SEM images of the four heat treat conditions evaluated for the Al 2219 formability study (100x SEM magnification).

Higher magnification SEM images were collected for each of the four conditions and are presented in Figure 27. These images better contrast the variability in size and distribution of both the smaller and large particles.

In all conditions, there is a bi-modal distribution of larger particles that are 5 - 50 µm in length versus smaller particles less than 5 µm. Qualitatively, in the AF condition there appears to be roughly an equivalent amount of small and large particles. Larger particles tend to be spherical or slightly elliptical in shape. The MT and AF conditions are very similar, even at higher magnification.

In HT1, there is a noticeable increase in the smaller particles (likely θ') compared to the AF condition. Additionally, the morphology of these smaller particles tends to be rod-shaped with high aspect ratio, which is significantly different from the generally spherical-shaped, low aspect ratio particles in the AF condition. Precipitation of finer second-phase (θ') particles is attributed to the rapid initial cooling rate in HT1 (suppressing the coarsening of θ), and subsequently slower cooling rate in the vicinity of the temperature range where θ' was reported to precipitate [14]. Given the desire of the O1-temper to increase the interparticle spacing, this heat treatment was not viewed as successful. It was evident that a slower cooling rate was required, leading to the parameter choice for HT2.

For HT2, the slower cooling rate resulted in a more desired microstructure consistent with the goal of the O1-temper. Very few small particles are present and the microstructure is dominated by larger particles (θ), which consists of a mix of spherical and elongated shapes. The smaller particles that are present tend to be spherical in shape, which differs from the observed predominately elongated shape of smaller particles in HT1. This difference in morphology may suggest that the smaller particles in HT2 are θ, compared to θ' in HT1. Interparticle spacing qualitatively appears to be the greatest in HT2 for all four conditions investigated.

Based on these observations of the particle sizes, distributions, and interparticle spacing, it is expected that HT2 would result in the most favorable condition for greatest formability.

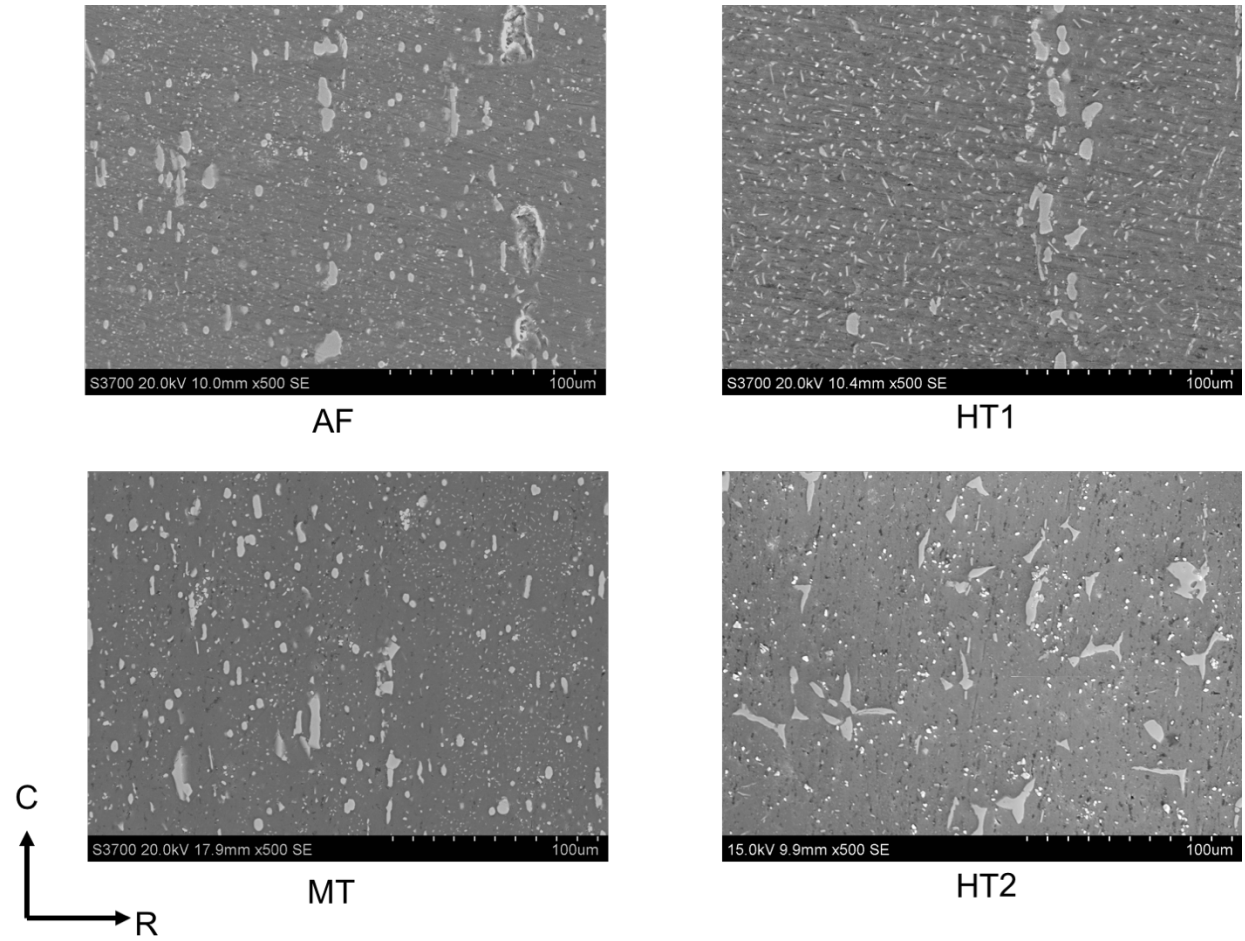

Figure 27. SEM images of heat-treated conditions at higher magnification (500x SEM magnification).

4.4. Tensile Testing to Evaluate Formability

Base Tensile Test Results

Tensile test results for the base region of ISC # 3 are shown in Table 3. Yield strength (YS), ultimate tensile strength (UTS), uniform elongation ($e_{uniform}$), elongation at specimen fracture (e_{max}), and strain hardening exponent (n) are reported. Values shown are the average of two specimens per orientation and condition. The base material represents the unformed, O-temper condition of

the Al 2219 preforms that Scot Forge provided to MT Aerospace. For comparison to the O-temper measured properties, handbook values from AMS 4031 are shown in Table 4 for Al 2219-O temper plate including maximum and typical properties [15].

The results indicate reasonable ductility in the starting condition of approximately 17 and 24 % for the axial and circumferential orientations of the ring. In the base, the axial orientation shows slightly higher YS (15.3 ksi) compared to the circumferential orientation (12.5 ksi). The higher YS and lower elongations values for the axial direction compared with the circumferential orientation indicate a greater degree of working in the axial direction during roll ring processing. According to Scot Forge, this is a common trend for rolled ring forgings. The lower YS and higher UTS for the circumferential orientation lead to an increased strain hardening exponent by nearly 50% compared to the axial orientation. The ductility and strain hardening exponent values demonstrate enhanced formability for the circumferential orientation compared to the axial direction. However, both directions exceed the minimum ductility quoted for 2219-O temper product in AMS 4031 [15], indicating that the condition Scot Forge delivered to MT Aerospace was acceptable.

Table 3. Al 2219 average tensile tests properties from base and wall regions of ISC #3 (AF condition). Data represent the average of two specimens in each condition and orientation.

Condition	Orientation	YS (ksi)	UTS (ksi)	$e_{uniform}$ (%)	e_{max} (%)	n
Base	Axial	15.3	26.6	14.14	16.68	0.1702
Base	Circumferential	12.5	27.3	17.07	23.87	0.2439
Wall	Axial	29.4	33.8	4.12	7.54	0.0602
Wall	Circumferential	27.7	32.0	4.06	13.18	0.0656

Table 4. Al 2219-O temper (0.02 to 2.0-inch-thick) plate properties from AMS 4031 [15] and Aerospace Structural Metals Handbook [16].

	YS (ksi)	UTS (ksi)	e_{max} (%)
Max strength / Min elongation	16 (max)	32 (max)	12 (min)
Typical	11	25	18

R-ratio plots for the axial and circumferential test orientations in the base material are shown in Figure 28. The circumferential orientation is much closer to unity, indicating better formability and lower anisotropy than the axial test orientation. The axial orientation values are significantly lower in the vicinity of 0.5. Lower R-values in the axial test specimens indicate stronger localization potential in the radial (thickness) direction. This may provide some indication of why filling the stiffeners presents a greater challenge with this process, particularly when taking into account that differential material flow rates may increase tensile stresses in the axial direction similar to this test orientation. The lower R-ratio values in the axial direction compared to the circumferential direction are likely impacted by the preferential alignment of stringer particles in the circumferential direction, which have the potential to form cracks. Axial tensile stresses would be favorable for crack growth along the circumferentially aligned stinger particles based on fracture mechanics principles.

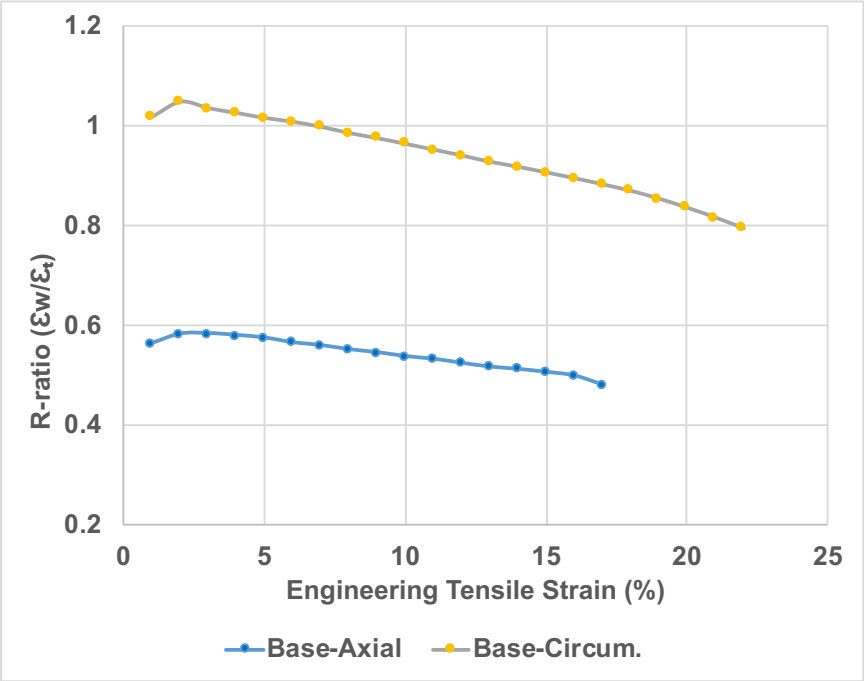

Figure 28. R-ratio plots for base tensile specimens. Data represent the average of two specimens in each orientation.

Wall Tensile Test Results

Tensile specimens were extracted from the wall region of test #3 and tested in the A and C orientations in the as-formed condition. No additional heat treating was conducted. In this state, the remaining ductility is reduced by ~ 50 % from the starting O temper condition in the base region (see Table 3). Maximum tensile elongations were measured to be approximately 7.5 and 13 %, respectively for the axial and circumferential orientations. The extent of uniform elongation was reduced to 4 % in each orientation. YS is significantly higher, as expected, in this condition due to the cold work imparted during forming. Hence, the extent of strain hardening during tensile testing is greatly reduced, as indicated by the strain hardening exponent decrease by a factor of 3 to 4x. In this condition, the remaining formability of the wall has been significantly reduced in the axial direction. In the stiffener sections, greater deformation has occurred due to higher stresses and increased material movement to fill the grooves on the mandrel as supported by the extensive cracking in those regions. The metallurgical evaluation in prior sections showed minimal particle cracking in the wall compared to the stiffener. One can assume that ductility values would be far lower in the stiffener material.

The far more limited remaining ductility in the wall tensile specimens in the axial direction point to the impact of the large, stringer particles. The microscopy images indicated chains of large particles aligned in the circumferential direction. Based on simple fracture mechanics considerations, tensile loading in the axial direction, perpendicular to the stringer particles aligned in the circumferential direction, provides a driving force for crack growth along those stringer particles. The driving force for cracking is much lower when the particles are aligned parallel to the tensile axis as in the case of the circumferential tensile specimens, leading to lower likelihood of propagation. Process and material optimization are required to improve formability and material flow in future campaigns to eliminate crack formation.

R-ratio plots for the axial and circumferential wall specimens from test #3 are shown together in Figure 29. These values are all lower than the R-values obtained in the same test orientations within the base material, indicating a reduction in formability and greater anisotropy. This is expected as deformation that occurred during forming of the wall will ultimately reduce the remaining ductility of that material.

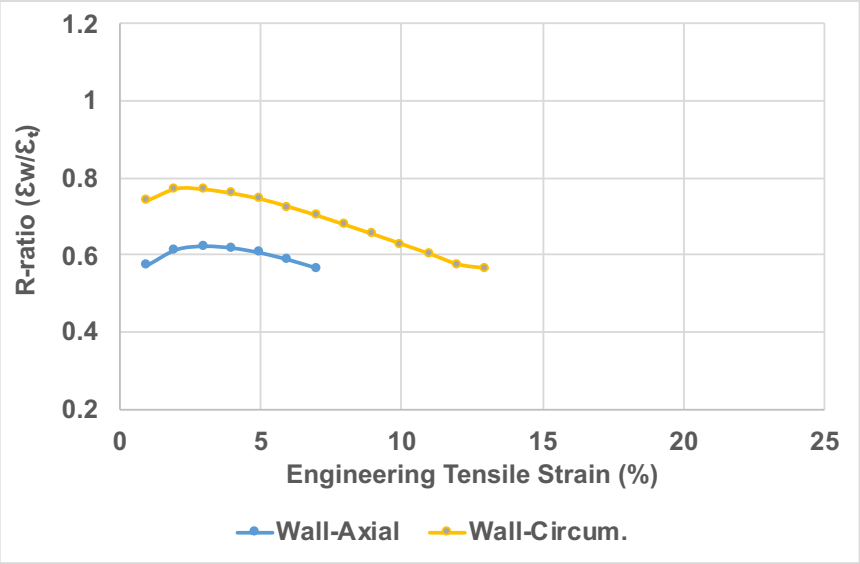

Figure 29. R-ratio plots for wall tensile specimens. Data represent the average of two specimens in each orientation.

O1 Temper Heat Treatment Results

From the preliminary heat treatment study on regions from test #4, it was apparent that HT2 – the O1 temper heat treatment with the slowest cooling rate – produced a microstructure with the greatest interparticle spacing, which is the intent of the O1 treatment. It was recognized that the AF and MT variants of the O-temper anneal yielded similar microstructures. Thus, tensile specimens were only tested in two of the 4 heat treated conditions: the as-received standard O-temper condition (AF), and the HT2 condition.

The tensile properties for the HT2 condition are shown in Table 5. Results for the AF condition previously shown in Table 3 are repeated in Table 5 for comparison. The elongation values agree within 2 % or less and the AF condition slightly outperforms the HT2 condition in each orientation. There is a noticeable decrease of ~ 50 % in YS and ~ 25 % in UTS for the HT2 condition compared to the AF condition in both test orientations, indicating that this is a much softer starting condition for forming. As a result of the softer starting condition, it exhibits a higher work hardening rate, supported by the greater strain hardening exponent values. Generally, higher n-values are desirable for greater formability. However, the lower elongations values negate that factor.

Table 5. Al 2219 average tensile tests properties from base region of ISC #3 in the HT2 condition. Data from the AF condition is repeated for comparison purposes. Data represent the average of two specimens in each condition and orientation.

Condition	Orientation	YS (ksi)	UTS (ksi)	$e_{uniform}$ (%)	e_{max} (%)	n
Base-AF	Axial	15.3	26.6	14.14	16.68	0.1702
Base-AF	Circumferential	12.5	27.3	17.07	23.87	0.2439
Base-HT2	Axial	7.4	21.5	14.64	16.09	0.2951
Base-HT2	Circumferential	7.3	21.7	16.66	21.17	0.2944

R-ratio plots for base material in the AF and HT2 conditions in the axial and circumferential test orientations are show in Figure 30 and Figure 31, respectively. In both orientations, the R-values are lower in the HT2 vs. the AF base material, indicating greater plastic anisotropy with respect to formability. The lower R-values for each orientation indicate a tendency for increased thinning and localized deformation in the radial direction (thickness direction of the tensile specimens). Hence, given the observed cracking experienced in the ISC forming trials within the stiffeners, poorer formability in the radial direction will lead to worse stiffener forming and likely a greater extent of cracking within the stiffeners. Therefore, it is determined that the lower ductility and greater propensity for localization in the radial (thickness) direction exhibited by HT2 are not desirable for ISC forming. The standard O-temper heat treatment provides improved formability, relative to the O1 temper heat treatment.

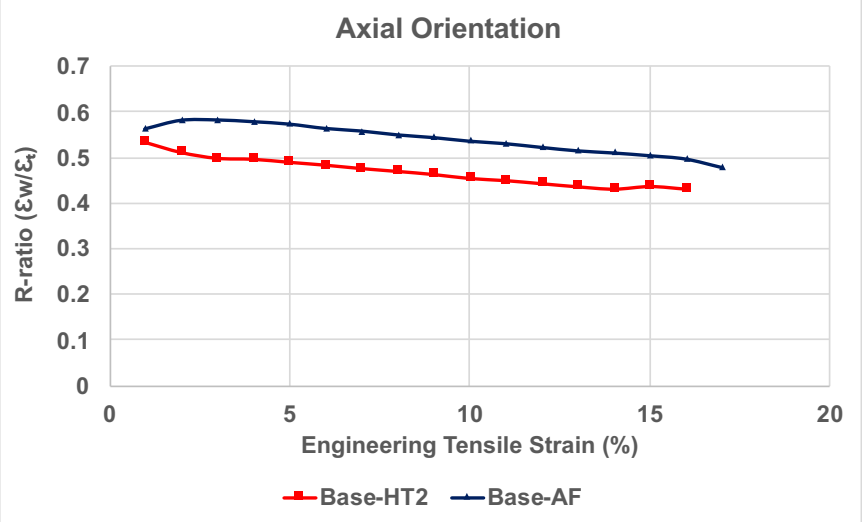

Figure 30. R-ratio plots for the AF and HT2 conditions for base region axial tensile specimens. Data represent the average of two specimens in each condition and orientation.

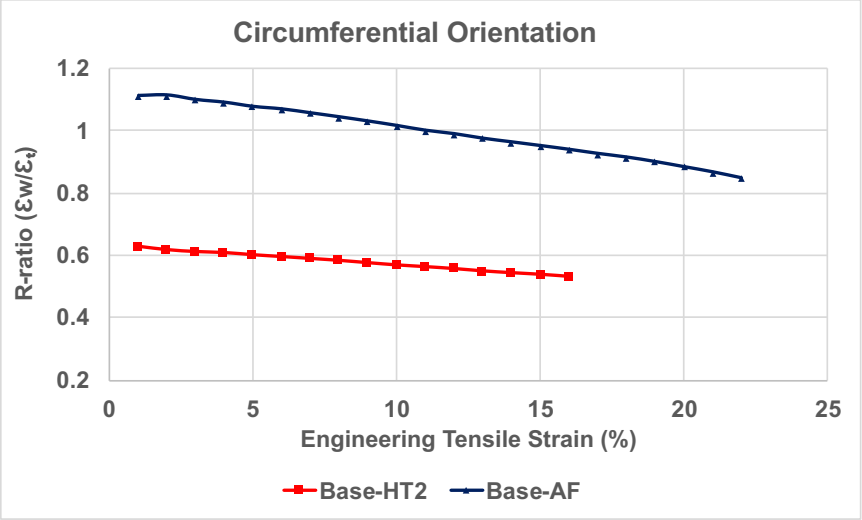

Figure 31. R-ratio plots for the AF and HT2 conditions for base region circumferential tensile specimens. Data represent the average of two specimens in each condition and orientation.

5. Summary and Conclusions

The ANNST Project successfully demonstrated the manufacturing feasibility of the Integrally Stiffened Cylinder (ISC) Process in 2017. However, further manufacturing development is required to fully optimize the process toward commercialization and the production of defect-free ISCs. NASA LaRC conducted metallurgical analysis and mechanical testing to characterize some of the issues experienced in the 2017 forming campaign to guide material and processing modifications in future manufacturing campaigns. The results of the characterization study revealed several key factors summarized below that contributed to cracking in the Al 2219 ISCs.

The Al 2219 exhibited insufficient formability particularly within stiffener locations. Evaluation of as-formed material revealed a fine-grained microstructure indicative of a grain structure that would be preferred for good formability. However, the excess Cu solute led to the formation of large, intermetallic, Al_2Cu particles common to Al-Cu alloys like Al 2219. Metallurgical examination revealed a high population of large, constituent particles with preferred alignment in long chains in the circumferential direction. These particles are sites of higher stress concentration and are prone to cracking both through particles and at particle/matrix interfaces. This was most noticeable in the stiffener regions where the highest stresses are anticipated and was a reason for the observed cracking within the stiffeners. Microcracks at individual particles coalesced with other cracks around neighboring particles to form larger cracks in the stiffeners. Thus, the inherent material condition containing large particles is unfavorable for forming as internal stresses increase.

Tensile testing revealed that for both the axial and circumferential orientations the ductility of the as-formed wall was roughly 50% lower than for the unformed base region. This is attributed to the large particles aligned in the circumferential direction, normal to the tensile axis for the axial test orientation. These particles likely originate during ingot processing and are largely unaffected by heat treatment. To correct this issue, the ingot processing practices need to be modified to suppress the formation of these large particles in favor of a homogeneous distribution of smaller particles (ideally spherical particles of less than 5 μm in diameter). Another option is to examine

other aluminum alloys with lower solute and impurity levels and hence lower likelihood of containing large particles. A microstructure with minimal to no large particles should exhibit improved formability compared to the Al 2219 material used in this forming campaign.

There were signs of inadequate lubrication along the edges of the stiffeners due to stick-slip friction between the stiffeners and mandrel grooves. Fissures were found on one side of stiffeners, indicating lubrication issues during forming. This promoted high stress concentrations and sub-surface cracking seen along that side of the stiffener. Cracking was further exacerbated by large Al_2Cu stringer particles, which are favorable for crack nucleation and propagation. The severity of the lubrication issues relative the extent of cracking observed in the ISCs is unclear. However, other manufacturing experts argue the effect of friction may be a stronger driving force for cracking and poor formability than the material issues associated with the larger particles. Certainly, reducing friction during forming will lower stresses within the part and ultimately enhance the odds for successful forming. As a result, new lubricants are being explored for subsequent forming campaigns and experts at the lubricant manufacturer are consulting with MT Aerospace to correct any issues.

As a result of these findings two suggestions have been made to improve formability. First, a new lubricant has been recommended for future forming trials as a more appropriate formulation for flow forming stiffeners. Second, for future forming trials, other higher formability aluminum alloys should be considered. Particularly those with minimal large, constituent particles for improved ductility.

Additionally, future efforts should focus on developing a machine specifically designed for ISC fabrication, which may include the ability to heat the part during forming, and accommodate different forming roller configurations / designs. The machine being used for the 10-ft. diameter forming trials is not designed for ISC fabrication. Instead, it is used to fabricate smooth-wall, steel cylinders. A dedicated ISC machine is estimated to cost $8 M, far in excess of current project budgets and likely will require industry investment.

References

1. Stoner, M. C., A. R. Hehir, M. L. Ivanco, and M. S. Domack. “Cost-Benefit Analysis for the Advanced Near Net Shape Technology (ANNST) Method for Fabricating Stiffened Cylinders.” *NASA/TM–2016-219192*, 2016.
2. Domack, M., J. Wagner, and W. Tayon, *NASA Fact Sheet: Innovative Manufacturing of Launch Vehicle Structures — Integrally Stiffened Cylinder Process*. NASA Game Changing Development Program Office. https://gameon.nasa.gov/advanced-near-net-shape-technology-annst/, accessed September 2018.
3. Davis, J. R., ed. *Aluminum and Aluminum Alloys*. ASM International: Materials Park, OH. 1993.
4. *Aerospace Material Specification 2770H: Heat Treatment of Wrought Alumunum Alloy Parts*. SAE International. Warrendale, PA, 2010.
5. Designation E8: Tension testing of metallic materials. *Annual Book of ASTM Standards Vol. 3.01*. American Society for Testing and Materials. West Conshohocken, PA, 2010.
6. Ghosh, A. K., “The Influence of Strain Hardening and Strain-Rate Sensitivity on Sheet Metal Forming.” *Journal of Engineering Materials and Technology*. **99**(3): p. 264-274. 1977.
7. Kleemola, H. J. and M. A. Nieminen, “On the strain-hardening parameters of metals.” *J Metallurgical Transactions*. **5**(8): p. 1863-1866. 1974.

8. Designation E646: Standard Test Method for Tensile Strain-Hardening Exponents (n - Values) of Metallic Sheet Materials. *Annual Book of ASTM Standards Vol. 3.01*. American Society for Testing and Materials. West Conshohocken, PA, 2010.
9. Designation E517: Standard Test Method for Plastic Strain Ratio r for Sheet Metal. *Annual Book of ASTM Standards Vol. 3.01*. American Society for Testing and Materials. West Conshohocken, PA, 2010.
10. Hecker, S. S., "Formability of Aluminum Alloy Sheets." *Journal of Engineering Materials and Technology*. **97**(1): p. 66-73. 1975.
11. Lege, D. J., F. Barlat, and J. C. Brem, "Characterization and modeling of the mechanical behavior and formability of a 2008-T4 sheet sample." *International Journal of Mechanical Sciences*. **31**(7): p. 549-563. 1989.
12. Kuziak, R., R. Kawalla, and S. Waengler, "Advanced high strength steels for automotive industry." *Archives of Civil and Mechanical Engineering*. **8**(2): p. 103-117. 2008.
13. Papazian, J., "Calorimetric Studies of Precipitation and Dissolution Kinetics in Aluminum Alloys 2219 and 7075." *Metallurgical Transactions A*. **13**(5): p. 761-769. 1982.
14. Papazian, J., "A calorimetric study of precipitation in aluminum alloy 2219." *Metallurgical Transactions A*. **12**(2): p. 269-280. 1981.
15. *Aerospace Materials Specification AMS 4031*. SAE International. Warrendale, PA, 2017.
16. Brown, W. F. and S. Setlak, eds. *Aerospace Structural Metals Handbook*. 39 ed. Vol. 6. CINDAS/USAF CRDA Handbook Operation, Purdue University: West Lafayette, IN. 2005.

REPORT DOCUMENTATION PAGE

Form Approved
OMB No. 0704-0188

1. REPORT DATE *(DD-MM-YYYY)*	2. REPORT TYPE	3. DATES COVERED *(From - To)*
1-03-2019	Technical Memorandum	

4. TITLE AND SUBTITLE

Characterization of 10-ft. Diameter, Aluminum Alloy 2219 Integrally Stiffened Cylinders

5a. CONTRACT NUMBER

5b. GRANT NUMBER

5c. PROGRAM ELEMENT NUMBER

6. AUTHOR(S)

Tayon,Wesley A.; Domack, Marcia S.; Wagner, John A.

5d. PROJECT NUMBER

5e. TASK NUMBER

5f. WORK UNIT NUMBER

057942.04.21.23

7. PERFORMING ORGANIZATION NAME(S) AND ADDRESS(ES)

NASA Langley Research Center
Hampton, VA 23681-2199

8. PERFORMING ORGANIZATION REPORT NUMBER

L-21006

9. SPONSORING/MONITORING AGENCY NAME(S) AND ADDRESS(ES)

National Aeronautics and Space Administration
Washington, DC 20546-0001

10. SPONSOR/MONITOR'S ACRONYM(S)

NASA

11. SPONSOR/MONITOR'S REPORT NUMBER(S)

NASA-TM-2019-220260

12. DISTRIBUTION/AVAILABILITY STATEMENT

Unclassified-
Subject Category 26
Availability: NASA STI Program (757) 864-9658

13. SUPPLEMENTARY NOTES

14. ABSTRACT

The integrally stiffened cylinder (ISC) process, pioneered by NASA Langley Research Center, offers significant savings for launch vehicle structures. The ISC process is a near net shape, advanced manufacturing method for fabrication of single-piece, thin-walled barrels with internal longitudinal stiffeners, eliminating the need for longitudinal welding and machining. A cost-benefit analysis of the ISC process estimated a 50% reduction in manufacturing costs and a 10% weight savings over the current multi-piece, machined and welded construction approach for stiffened barrels. In 2017, commercial-scale manufacturing trials were pursued, leading to a successful manufacturing demonstration of 10-ft. diameter ISC barrels fabricated from Al alloy 2219. Some cracking was observed in the stiffeners during fabrication. Optical metallography was performed to evaluate the as-formed microstructures to identify potential causes of cracking, along with mechanical testing to evaluate formability. Results revealed that cracking in the stiffeners was attributed to three likely causes: 1) large Al-Cu stringer particles, 2) stick-slip friction between the mandrel and ISC due to non-optimized lubrication, and 3) differences in material flow rate between the wall and stiffener locations. Testing to gauge formability revealed a significant decrease in ductility in the longitudinal directional for the as-formed condition, attributed to reduced ductility due to the large Al-Cu stringer particles.

15. SUBJECT TERMS

Advanced manufacturing; Al alloy 2219; Cryogenic tanks; Integrally Stiffened Cylinder (ISC) Process; Near net shape

16. SECURITY CLASSIFICATION OF:			17. LIMITATION OF ABSTRACT	18. NUMBER OF PAGES	19a. NAME OF RESPONSIBLE PERSON
a. REPORT	b. ABSTRACT	c. THIS PAGE			STI Help Desk (email: help@sti.nasa.gov)
U	U	U	UU	41	19b. TELEPHONE NUMBER *(Include area code)* (757) 864-9658